We are IntechOpen, the world's leading publisher of Open Access books Built by scientists, for scientists

4,800
Open access books available

122,000
International authors and editors

135M
Downloads

Our authors are among the

154
Countries delivered to

TOP 1%
most cited scientists

12.2%
Contributors from top 500 universities

WEB OF SCIENCE™

Selection of our books indexed in the Book Citation Index in Web of Science™ Core Collection (BKCI)

Interested in publishing with us?
Contact book.department@intechopen.com

Numbers displayed above are based on latest data collected.
For more information visit www.intechopen.com

Chapter 8

High-Density Plasma-Enhanced Chemical Vapor Deposition of Si-Based Materials for Solar Cell Applications

H. P. Zhou, S. Xu and S. Q. Xiao

Additional information is available at the end of the chapter

http://dx.doi.org/10.5772/63529

Abstract

High-quality and low-cost fabrication of Si-based materials, in which many fundamental and technology problems still remain, have attracted tremendous interests due to their wide applications in solar cell area. Low-frequency inductively coupled plasma (LFICP) provides a new and competitive solution, thanks to its inherent advantages of high-density plasma, low sheath potential, and low electron temperature, etc. The plasma characteristic-dependent microstructures, optical and electronic properties of the LFICP CVD-based hydrogenated amorphous/microcrystalline silicon and silicon oxides are systematically studied. Remote-LFICP combing the high-density plasma nature of ICP and mild ion bombardment on growing surface in remote plasma allows the deposition of high-quality Si-based materials providing excellent c-Si surface passivation. The mechanism of surface passivation by LFICP CVD Si-based materials, interaction between plasma species and growing surface are analyzed in terms of the plasma properties. These results pave the way for LFICP CVD utilization in Si-based high-efficiency and low-cost solar cell fabrication.

Keywords: LFICP CVD, remote-plasma, Si-based materials, solar cells, passivation

1. Introduction

Plasma-enhanced chemical vapor deposition (PECVD) is an excellent alternative for depositing thin films at lower temperature than those utilized in a conventional CVD process. Plasma generated by a glow discharge absorbs the electrical energy, and hence the neutral gases were dissociated into reactive radicals, ion, neutral atoms and molecules, and other highly excited

species through the electron impact instead of conventional thermal energy. These atomic and molecular fragments interact with a substrate and, depending on the nature of these interactions, either etching or deposition processes occur at the substrate. Therefore, the substrate can be maintained at a lower temperature keeping the reactions for the thin-film deposition. These salient advantages of PECVD, i.e., low temperature nature, together with the high quality of the deposited films make PECVD be an important route for the fabrication of Si-based materials, which have been the dominant material system for the present solar cell research and commercial market. PECVD-based silicon nitride (SiN_x:H) with the feedstock gases of SiH_4 and NH_3 act as the passivation and antireflection layer of the bulk Si solar cells. Fabrication of Si thin-film solar cells consisting of the stack of p-, i-, and n-type hydrogenated amorphous/microcrystalline Si (a-/μc-Si:H) films also relies on PECVD technology. The interface quality and energy conversion efficiency of HIT (heterojunction with intrinsic thin layer) solar cell with the record efficiency of 25.6% [1] closely depends on the PECVD process because the symmetric intrinsic passivation layers and doped layers (front emitter and back surface field layers) are also prepared by PECVD technology [2].

Although PECVD-associated Si-based materials are dominant over other materials in present solar cell market, there are a variety of challenges due to the nature of the utilized PECVD method. The common PECVD uses the capacitively coupled plasma (CCP) between parallel plates driven by a 13.56 MHz RF power generator. The ionization degree of the neutral gas is at a low level of $\sim 10^{-6}$–10^{-4} because of the low electron density of $\sim 10^{9}$–$10^{10}/cm^3$ in a CCP discharge mode. In principle, this means a low deposition rate of the targeted materials. As a consequence, the deposition rate of PECVD-based a-/μc-Si:H is about 0.5 nm/s [3], which is not desirable for cost-efficient, thin-film solar cell productions. Furthermore, the intensive coupling of the plasma density and ion energy in CCP complicates the deposition of high-quality thin films and the achievement of high-efficiency solar cells because strong ion bombardment would result in excessive defect formation in the films and on the growing surface/interface, and hence significant deterioration of the energy conversion efficiency of the solar cells [4]. These disadvantages of PECVD can be partially remedied by using very high-frequency (VHF) PECVD, which can effectively decouple the plasma density and electron density due to the increasing electron input power fraction of the total input power with frequency [5, 6] and enhance the deposition rate. However, there is not any report on the higher efficiency of the VHF-PECVD-based solar cells [7].

High-density plasma represented by inductively-coupled plasma (ICP) has increasingly attracted more interests due to its wide application areas such as microelectronics, display, and solar cells, etc. The prominent advantage of high density of ICP makes it very appropriate for the deposition of Si-based materials (a-/μc-Si:H, silicon carbide, silicon oxide, and silicon nitride), which are widely used in solar cells. Although there are numerous reports on the ICP-based deposition of these materials, the as-deposited Si-based materials with low defect density and excellent interface features are few, not to mention the involved high-efficiency solar cells. We have been making many efforts on low-frequency (460 kHz) ICP (LFICP) excitation, characterization, and application in nano-fabrication [8] and a wide range of thin films' synthesis [9, 10]. A discharging photograph of the LFICP facility and its schematic

http://dx.doi.org/10.5772/63529

structure are shown in **Figure 1(a)** and **1(b)**, respectively. The power of the low-frequency power generator is coupled into the reactive chamber sealed by a quartz window via a matching/tuning unit to sustain the reactive gases discharge.

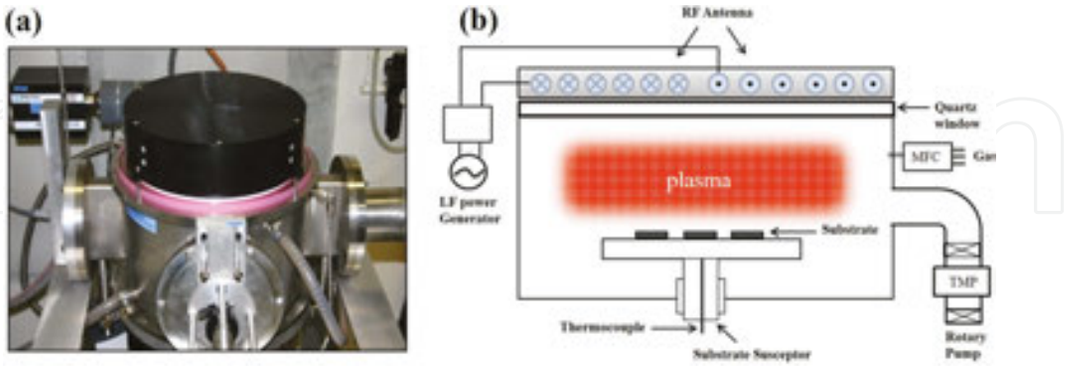

Figure 1. Discharging photograph of the LFICP facility (a), and its schematic structure (b).

In comparison with the conventional CCP source, the LFICP source has several prominent merits as follows [11, 12]: (i) high densities of the plasma species; in particular, the electron number density n_0 can reach 10^{13} cm^{-3} in the pressure range of a few pascal; (ii) low plasma sheath potentials of several or tens of volts, which are beneficial for the reduction in ion bombardment on the deposited films; (iii) low electron temperatures of a few electron volts in a broad range of discharge conditions; and (iv) excellent uniformity of the plasma parameters in the radical and axial directions. By using this novel plasma generator, Si-based materials have been fabricated with a high-deposition rate at low temperature. Hydrogenated, amorphous silicon carbide [13] (a-SiC_x:H, presently used as transparent doped layers in thin film and heterojunction solar cells) with a wide carbon component x (0.09–0.71) has been attained by adjusting the feedstock gas ratio of CH_4/SiH_4 dissociated by LFICP generator. Furthermore, low-temperature (500 °C) deposition of nanocrystalline SiC (nanocrystal size of about 6 nm) has been developed by using LFICP [14]. Low-temperature (100–200 °C) and high-rate (>1 nm/S) deposition of nc-Si in the direct plasma region of LFICP have been realized [15]. In our previous works [16, 17], it was also found that the severe etching on silicon surface directly exposed to the high-density hydrogen containing plasma drastically changes the morphology and microstructures of the surface. As a consequence, it is very easy to attain μc-/nc-Si:H with a high deposition rate. However, this high-density ion region is not suitable for solar cell fabrications where the defect density in the silicon films and on the interface need to be elaborately minimized in terms of the plasma characteristics. Apparently, the severe ion bombardment in a direct ICP would introduce additional defects reducing the photovoltaic performance of the solar cells. Remote-LFICP [18] is a feasible solution to avoid the ion bombardment damage on the surface through separating the plasma generation region and deposition region. High-density plasma of hydrogen gas is generated and mainly confined in the region near the antenna, i.e., the plasma generation region. The energetic species transport into the growth region and react with the injected SiH_4 neutral gas forming a variety of precursor radicals for the deposition of high-quality thin film at low temperatures.

High-quality Si-based materials have been attained by means of remote-LFICP:

1. As-deposited a-Si:H exhibits competitive surface passivation ability on crystalline silicon, thanks to the minimized inner and interface defect density [19];
2. Silicon nitride with controlled bandgap due to the excellent dissociation ability of LFICP facility was realized [20]. Meanwhile, the remote-LFICP-deposited silicon-rich a-SiN_x:H displays excellent Si surface passivation (surface recombination velocity of 36 cm/s for low resistivity n-type Si wafer) [21].
3. Remote-LFICP-based a-SiO_x:H provides effective surface passivation of low resistivity Si wafer (surface recombination of 70 cm/s obtained) [22].

The aim of this work is to systematically report the high-density plasma-enhanced chemical vapor deposition of device-grade Si-based materials by means of LFICP and its solar cell applications. The as-deposited Si-based materials will be studied in combination with the LFICP characteristics. Their soar cell applications mainly focus on the Si surface passivation using remote-LFICP-CVD-based Si-based materials. This article is organized as follows. Section 2 makes a brief introduction on a-/μc-Si:H and then focuses on the processing parameters dependent microstructures and properties of the LFICP-CVD intrinsic and doped a-/μc-Si:H thin films. Section 3 focuses on the applications of LFICP-CVD a-/μc-Si:H for c-Si surface passivation. The influence of the plasma characteristics on the properties of LFICP-based materials and growing surface properties are intensively investigated.

2. a-/μc-Si:H thin films

2.1. a-Si:H

Amorphous silicon (a-Si) is a solid-state material made of silicon atoms which are arranged in a short-range order. With the absence of the constraints of periodicity in elemental amorphous silicon, it is difficult for each silicon atom to be linked up with four others. Compared with crystalline silicon (c-Si), the average bond angles between nearest-neighboring atoms are distorted. Some bonds are even broken and result in so-called "dangling bonds". These two main defects of the lattice of a-Si:H, i.e., bond distortion and dangling bonds, create large densities of allowed states within the forbidden band gap in such a way that the material cannot be effectively doped N- or P-type and is not electronically useful. However, if the substance is hydrogenated, the hydrogen atoms saturate the dangling bonds and reduce the density of states within the forbidden gap. The bond distortion results in band tails near the valence and conduction bands. In these band tails, the electrons (or holes) are localized in space and do not directly participate in the electronic transport. The deep states near the middle of the band gap results from the non-passivated dangling bonds. These defect centers are "amphoteric"—there are three charge states, i.e., +e, 0, and –e charges, leading to two levels (transitions between the 0/+ and −/0 charge states). The dangling bonds act as recombination centers for free electrons and holes.

http://dx.doi.org/10.5772/63529

2.2. μc-Si:H

μc-Si:H is known to be a complex material consisting of crystalline and amorphous silicon phase plus grain boundaries [23]. **Figure 2(a)** shows a typical transmission electron microscopy (TEM) of μc-Si:H. Apparent columnar grains are observed. The crystalline growth starts at nucleation centers near the interface between film and substrate. During the competitive growth between the nucleation centers, the diameter of the remaining crystalline increases leading to the cone-shaped crystallites near the substrate surface [24]. **Figure 2(b)** displays the microstructure evolution from highly crystal μc-Si:H to amorphous a-Si:H. The highly crystal and amorphous structure are described in the left and right margin, respectively. From left to right, the column size decreases and more amorphous phase is introduced between the crystalline grains. This interrupts the columnar crystalline structure in the lateral direction.

Practically, μc-Si:H is closely related to a-Si:H, as the deposition technique for both materials is the same. However, the deposition parameters, such as discharge power density, working pressure, substrate temperature, etc., in the RF discharge deposition method, collectively determine the ultimate microstructures of the obtained silicon thin films. CCP-PECVD is the most widely studied technique for the deposition of a-/μc-Si:H films. In this technique, hydrogen-diluted silane is dissociated by electron impact from the RF field between two parallel plate electrodes to form SiH_x radicals and atomic hydrogen. The generated species diffuse/drift to the growing surface. The species and their reaction products are either incorporated into the growing film or are re-emitted from the surface into the gas phase. The radicals then undergo various secondary reactions during their transport to the substrate.

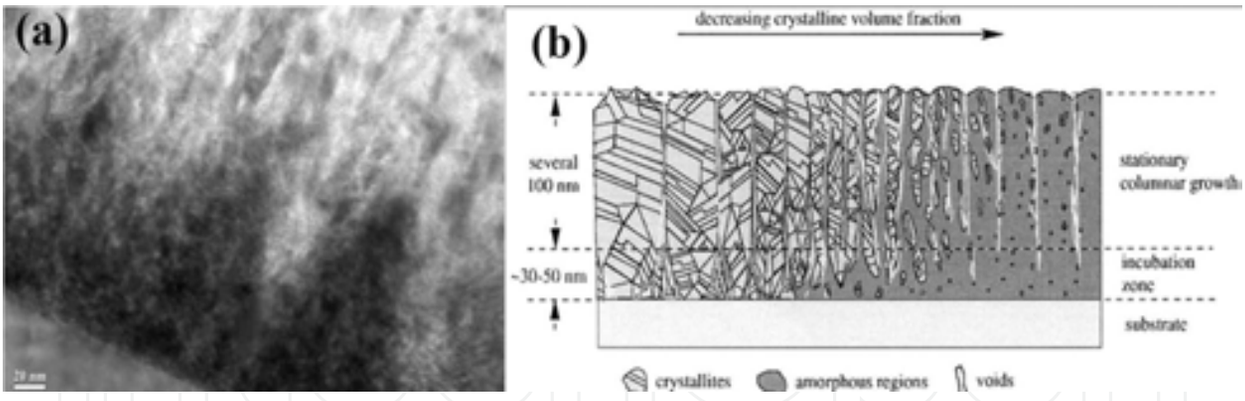

Figure 2. TEM micrograph of a μc-Si:H film grown on silicon substrate by means of LFICP (a), and a schematic drawing to show the microstructure evolution from μc-Si:H (left) to a-Si:H (right) (Reproduced from Ref. [24]).

2.3. a-/μc-Si:H by LFICP CVD

Although method of ICP has the advantages over the traditional CCP as demonstrated above, the reports on its applications in silicon thin-film deposition are not abundant, not to mention the solar cell fabrication. For reference, some main progresses are summarized as follows. Li et al. [25] used the built-in one-turn coil inductance antenna driven by 13.56 MHz RF power to fabricate μc-Si:H with tunable preferred orientation through controlling the hydrogen

dilution. By the similar method with external conductance coil power by the same frequency generator, Shen et al. [26, 27] obtained low defect density ((3 x 10^{15}/cm^3) a-Si:H films, from which a single-junction a-Si:H solar cell with energy conversion efficiency of 9.6% was successfully fabricated. The researchers from Hiroshima University realized the high-rate deposition (up to 4 nm/s) of μc-Si:H with a low-level defect density in the year of 2001 [28, 29]. They systematically studied the films' optoelectronic properties such as the optical band gap, dark and photo conductivity, defect density, crystalline fraction ratio, etc. It seems that as-deposited silicon films are device grade and fulfill the common requirements for solar cell fabrications. Unfortunately, they have not reported their subsequent achievements in their research. The reports on the application of ICP-grown silicon thin films in heterojunction solar cells are not available. The only related work on the surface passivation by ICP-grown a-Si:H was reported in Ref. [30], where minority carrier lifetime of 53 μs was obtained on a P-type silicon substrate (resistivity 1–20 Ωcm) with a 15-nm-thick a-Si:H passivation layer.

For ICP reactor, there are two types of antenna configurations, namely cylindrical and planar. The present LFICP driven by a low frequency of 460 kHz power generator belongs to a planar coil configuration. As mentioned above, high-density ion region in ICP is not suitable for a-Si:H thin-film deposition for silicon surface passivation due to the severe ion bombardment. In order to decrease the ion bombardment, the distance *d* between the antenna and the substrate stage is increased by extending the deposition chamber height. In the a-/μc-Si:H deposition, two distance values of 33 cm or 53 cm were adopted for comparison purpose. The dependence of a-/μc-Si:H film microstructure and properties on the deposition parameters were studied. The n-doped and p-doped μc-Si:H layer were obtained with the introduction of dopant gases of phosphine (PH_3) and diborane (B_2H_6), respectively. The electrical properties of the doped films were analyzed.

2.4. Discharge power effect

The a-Si:H/μc-Si:H thin films were deposited on the double-side polished silicon and glass substrates cleaned by standard methods. The sample holder was heated to a temperature of 140 °C monitored by an internally equipped thermal couple. The flux of silane (H_2) was kept constant at 5 sccm (20 sccm). The inductive RF discharge power was varied between 1.0–2.5 kW. The thicknesses of all the deposited thin films were measured directly from the cross-sectional scanning electron microscopy (SEM) image by using a JEOL JSM-6700F filed emission scanning electron microscope. The deposition rate can be calculated from the thickness divided by deposition duration. FTIR measurements were performed on a Perkin-Elmer FTIR 1725X spectrometer in the mid-infrared range from 400 to 4000 cm^{-1} with an increment of 1 cm^{-1}. The Cary 510 Bio spectrometer (300–1100nm) was used to measure the UV-VIS transmission spectra.

2.4.1. Optical band gap and deposition rate

The UV-VIS transmission spectra (shown in **Figure 3(a)**) of the thin films deposited on glass at different RF powers were measured to extract the parameter of optical band gap E_g. Evident interference fringes due to multi-layer interface reflections were observed in the spectra range

http://dx.doi.org/10.5772/63529

longer than the absorption edge. The absorption edge occurs a redshift with deposition power, indicating shrinkage of the optical band gap. The transmission T was transformed into absorption α by the relation of $\alpha \infty$-ln(T) using the thickness of the films directly read from the cross-sectional SEM images. The optical band gap E_g of a-/μc-Si:H (Si an indirect band gap semiconductor) can be deduced from the Tauc equation

$$h\gamma\alpha(h\gamma)=B(h\gamma - E_g)^2 \quad (1)$$

where B is the edge width parameter related to the width of band tails in the film [31], and $h\nu$ the photon energy. In general, B factor is also taken as a measure of the overall structural disorder and a higher value for B would indicate a lower degree of structure disorder [32]. In our calculation, the obtained value of B (>800 $cm^{-1/2}.eV^{-1/2}$) is larger than that of literatures, indicating less disorder and defects in the thin films.

The obtained E_g as a function of applied RF power together with the average deposition rate are both plotted in **Figure 3(b)**. A transition point of E_g was observed at power of 1.8 kW. Below 1.8 kW, E_g encounters a decrease from 2.30 eV for 1.0 kW to 2.10 eV for 1.8 kW. On the contrary, E_g increases from 2.10 eV for 1.8 kW to 2.14 eV for 2.5 kW. This changing trend of E_g is related to the crystallinity of the thin films and the hydrogen content, which will be discussed below based on the experiments of Raman scattering and FTIR. The increasing RF power results in the steady increase in the average deposition rate from 7 to 21 nm/min. These values obtained at antenna-substrate distance d of 33 cm are about half of those corresponding to distance of 11 cm [33].

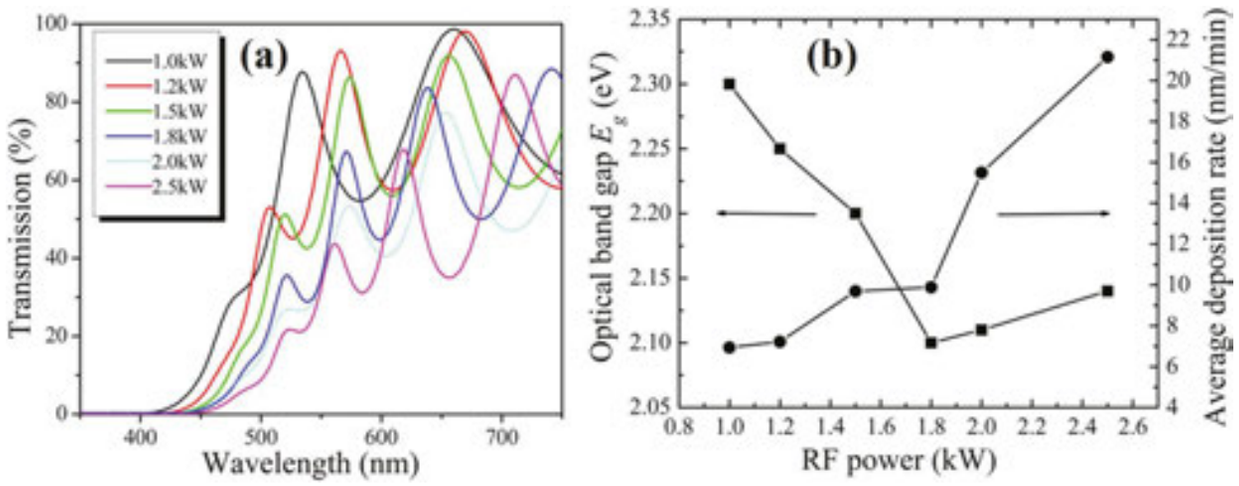

Figure 3. The UV transmission spectra of the thin films deposited at different RF powers on glass substrate (a), and deduced E_g (filled squares) and average deposition rate (filled circles) (b).

Another feature of the present films is the higher optical band gap E_g than that reported in Refs. [34–36] where E_g was obtained by the methods other than Tauc method (spectroscopic ellipsometry and surface photovoltage spectroscopy).

Although it was recognized that the Tauc method will lead to a larger value for E_g, it will give a correct variation trend of the value with respect to an independent parameter like RF power, substrate temperature, and so on. Herein, the values of E_g are above 2 eV, larger than the values (<1.9 eV) [33] obtained in earlier works performed on the direct-plasma ICP system with other similar deposition parameters. This should be correlated to the increased hydrogen content (following FTIR results) in the thin films.

2.4.2. Raman scattering and crystallinity of the thin films

The micro-Raman scattering experiments were performed to estimate the crystal phase information in the thin films. The obtained spectra are displayed in **Figure 4(a)**. It was observed that the dominant peak gradually shifts from (480 to (520 cm^{-1} through a mixed phase state at the power of 1.8 kW. This change reflects phase evolution from completely amorphous to highly crystal with an applied RF power in the films. In fact, the crystallinity value can be estimated by using different methods described in Ref. [37]. In this work, the method based on Gaussian line fitting [38] is used, where I_a

$$fc = (I_c + I_i) / (I_a + I_c + I_i) \tag{2}$$

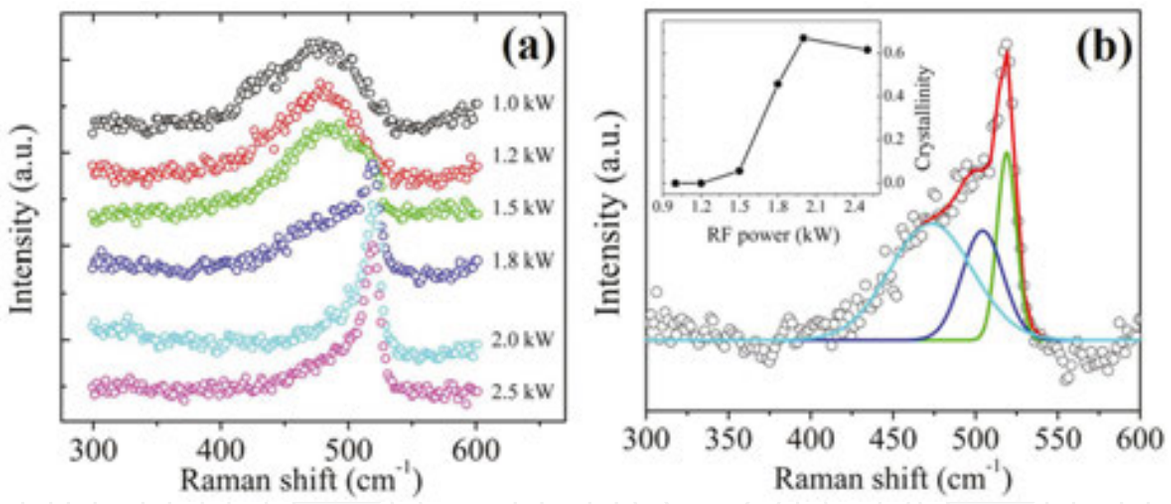

Figure 4. RF power-dependent Raman scattering spectra (a), and the Gaussian-shaped curve decomposition of the Raman spectrum in the thin film deposited at RF powers of 1.8 kW. The inset of (b) shows the RF power-dependent crystallinity of the thin films.

I_i, and I_c are the integrated area of each phase, i.e., the amorphous ((480 cm^{-1}), intermediate ((510cm^{-1}), and crystalline phase ((520 cm^{-1}), respectively, in the Raman spectra. A typical deconvolution result is shown in **Figure 4(b)**, where the cyan, blue, and green curves (from left to right) denote the amorphous, intermediate, and crystal component, respectively. The experimental (open circle) and overall fitting result agrees well, indicating the validity of the deconvolution procedure. The calculated crystallinity as a function of RF power is included in the inset of **Figure 4(b)**. As expected, the crystallinity increases monotonously in the power

http://dx.doi.org/10.5772/63529

range of 1.0–2.0 kW because of the production of denser and more energetic ion/radicals in the plasma and area near the surface of the substrate. Higher plasma density means more frequent impacts between the electron and the precursor gases, and thus a larger deposition rate. More energetic ion/radicals imply that the adsorbed radicals on the surface will have a greater diffusion length. This assists the adsorbed radicals to reach the most energetically favorable sites and gives rise to better crystallization of the synthesized thin films [39]. The crystallinity decreases from 67.0 to 61.6% when the RF power is further increased from 2.0 to 2.5 kW. This should be related to the rapid increase of deposition rate in the range of 2.0–2.5 kW shown in **Figure 3(b)**. One possible interpretation may be that: a higher (>2.0 kW) RF power excites more and more precursor ions like SiH, SiH_2, and SH_3 to improve the growth rate; on the other hand, the overly rapid growth minimizes the hydrogen etching effect on the existing weak and strained Si bonds. It is generally accepted that hydrogen etching is also an important mechanism to improve the crystallinity of Si thin films [40].

2.4.3. FTIR and hydrogen content in the thin films

The FTIR spectra of the thin films deposited with various RF power are shown in **Figure 5(a)**. Within a wavenumber range of 500–2300 cm^{-1}, three Si-H bond-related bands were observed. The first one, located at around 640 cm^{-1} was unambiguously attributed to Si-H rocking/wagging mode. Its exact location gradually changed from 644 to 630 cm^{-1} with increasing RF power as displayed in **Figure 5(b)** (the filled circles). This is also correlated to the phase evolution from amorphous to crystal silicon [41]. The second one comprising of two sub-peaks located at 845 and 890 cm^{-1} were identified as the bending mode of dihydrides SiH_2 [41]. The third one at the region of (2100 cm^{-1} is recognized as the SiH_x stretching mode. One can see that these hydrogen-related signals become weak with increasing RF power, implying the decreasing bonded hydrogen content in the thin films. Actually, the bonded hydrogen content in the thin films can be estimated from the Si-H bond rocking/wagging mode using the following equation:

$$C_H = A_\omega \int \frac{\alpha(\omega)}{\omega} d\omega = A_\omega I_\omega \tag{3}$$

where the oscillator strength A_ω is of value of 1.6×10^{19} cm^{-2}. The calculated hydrogen content at.% (defined as density ratio of hydrogen to that of hydrogen plus silicon) versus applied RF power is plotted as filled square in **Figure 5(b)**. The hydrogen content is in the range of 7.9–-17.4% and exhibits a general decreasing trend with RF power. Meanwhile, much lower values (<8%) were obtained using the same method in the case of direct plasma (i.e., the film deposition region located in the plasma generation region) [15, 33]. A local fluctuation of hydrogen content was also observed at a power of 1.8 kW, where the thin film is of transition state from amorphous to crystal phase. Further increase in RF power from 2.0 to 2.5 kW leads to a little improvement of hydrogen content, which is consistent with the decreasing crystallinity in this power range shown in **Figure 4(b)**.

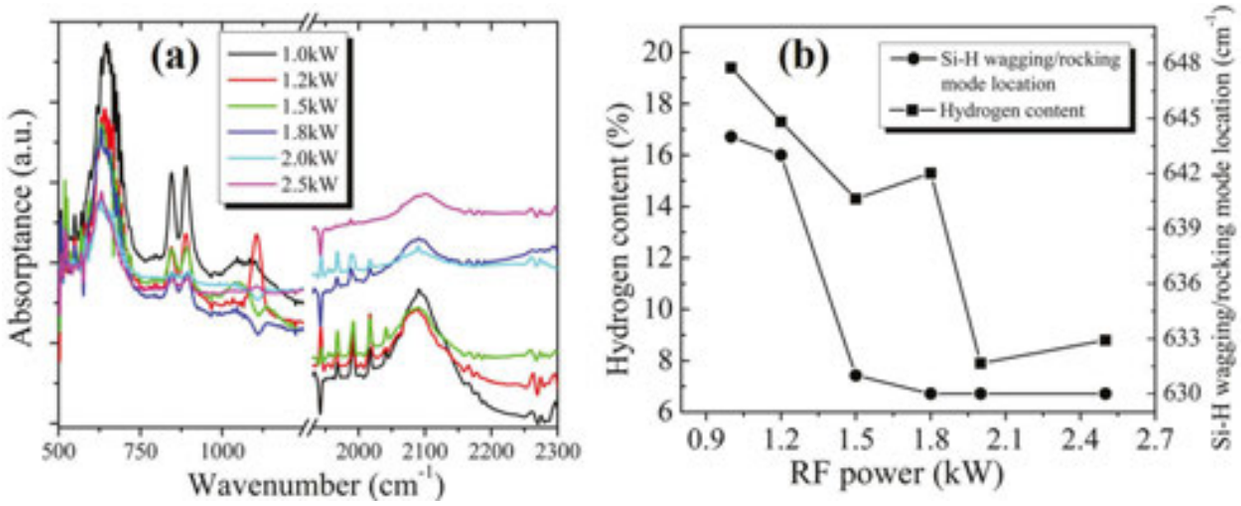

Figure 5. FTIR absorption spectra of the thin films deposited at different RF powers (a), and the RF power-dependent hydrogen content (filled squares) and Si-H wagging/rocking mode location (filled circles) (b).

2.5. Hydrogen dilution effect

Hydrogen in the deposited films originates from the diluent hydrogen gas and hydrogen atom bonded in silane molecules. From the point view of the deposition process, hydrogen facilitates the dissociation of silane through increasing the ion/electron impact, influences the surface energy of the growing surface via terminating the surface silicon atom, and etches the growing surface. Therefore, the hydrogen dilution should have a substantial effect on the microstructures of the ultimate silicon thin films. In this set, the RF discharge power and substrate are fixed at 1.5 kW and 140 °C, respectively. The total flow rate of SiH_4 and H_2 is kept at 20 sccm. The respective flow rate of SiH_4 and H_2 are changed with varying dilution ratio $[H_2]/[SiH_4]$ = 0, 0.25, 0.5, 1, 2, 3, and 4. The working pressure in the deposition chamber is kept at 7.2 Pa.

Figure 6 shows the average deposition rate and E_g deduced from the Tauc method described above. As expected, the deposition rate monotonically decreases with the decreasing silence concentration (i.e., increasing hydrogen dilution ratios). When the dilution ratio changes from 0 (pure silane) to 4, the deposition rate drops sharply from 42 nm/min to 10 nm/min. However, the case of E_g is more complicated with increasing dilution ratios. Within the range of ratio 0–2, E_g increases from 2.17 to 2.32 eV. Further increase in dilution ratio results in decreasing E_g. At a dilution ratio of 4, E_g is 2.21 eV. It has been mentioned above that E_g of a-/μc-Si:H is related to the crystallinity and hydrogen content in the films. The corresponding Raman spectra shows that all the films deposited under present conditions are of amorphous structure without clear crystalline fractions. As pointed out above, the wagging/ rocking mode location in FTIR spectra is also related to the phase configuration in the films.

http://dx.doi.org/10.5772/63529

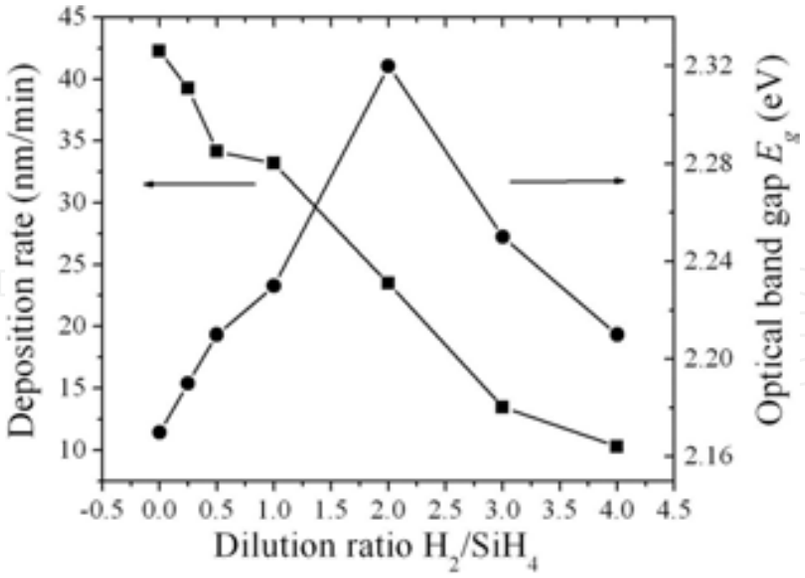

Figure 6. Dilution ratio-dependent optical band gap and average deposition rate.

Figure 7 shows the extract waging/rocking vibration mode. With a small amount of hydrogen introduction (H_2/SiH_4 = 0.25), the hydrogen content C_H increases from 26.3 to 27.5% and the wagging/rocking mode location shifts from 649 to 644 cm^{-1}. C_H drastically drops to 24.4% at a dilution ratio of 0.5. The values of C_H and the location of wagging/rocking mode are comparably steady in the dilution range of 0.5–2. Beyond 2, C_H decreases drastically to 12.2% and the mode location shifts to 631 cm^{-1} at a ratio of 4. The location shift to the small wavenumber side with increasing dilution ratios implies the phase evolution to the crystalline orientation.

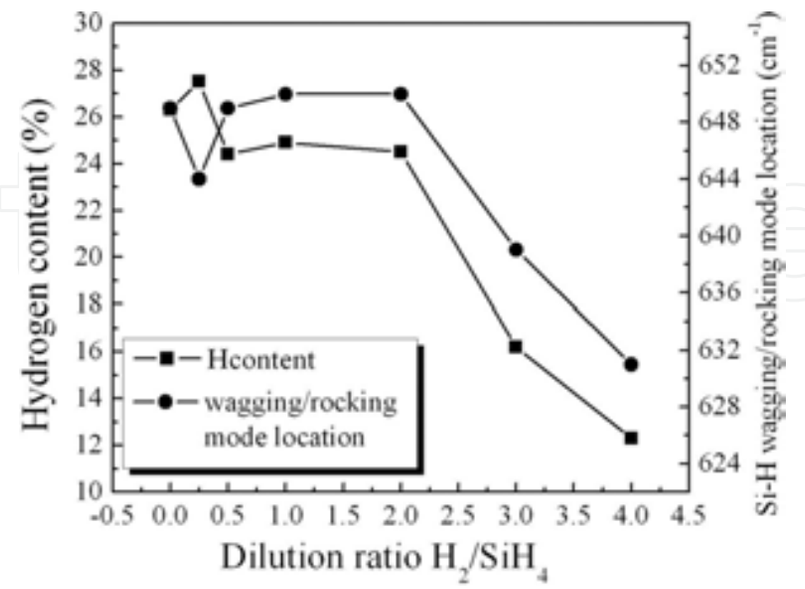

Figure 7. Hydrogen content and the wagging/rocking mode location in the a-Si:H films as functions of the dilution ration H_2/SiH_4.

In view of the above experimental results, hydrogen dilution in LFICP method is also a key parameter influencing the hydrogen content C_H in the films. However, its effect on the crystallinity of the films is less pronounced than that of the discharge power.

2.6. Working pressure effect

One of the inherent features of LFICP is low working pressure up to several tens of Pa. In this section, the working pressure is altered in the range (1–19Pa) enabling a stable discharge. The discharged power was kept at 2.5 kW. No external heating was applied to the substrate. The flow rate of SiH_4 and H_2 are 12.5 sccm. The Raman scattering experiments revealed the amorphous structure of these films. **Figure 8** displays the working pressure-dependent E_g and average deposition rate. The deposition rate monotonically increases with working pressure from the 68 nm/min (1 Pa) to 142 nm/min (19 Pa). On the contrary, E_g becomes narrower with working pressure: 2.34 eV for 1 Pa, and 1.92 eV for 19 Pa.

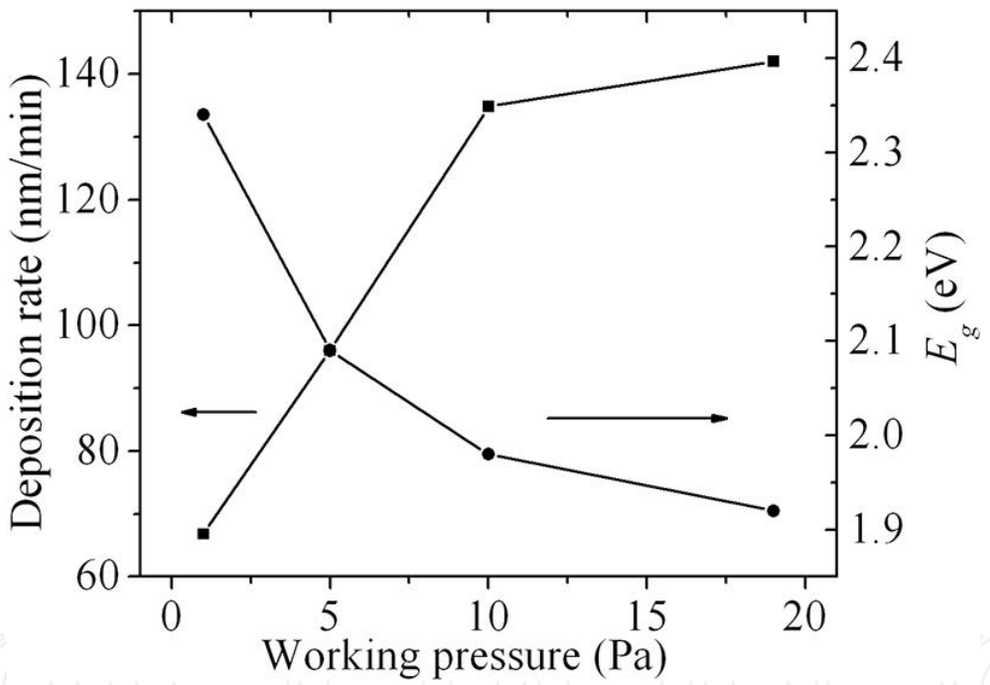

Figure 8. The deposition rate and E_g as functions of working pressure.

Figure 9(a) shows the FTIR absorbance spectra of these films. The intensity of the waging/rocking mode becomes weaker with increasing work pressure, indicating the effusion of the bonded hydrogen with increase in the working pressure. The detailed hydrogen content as a function of working pressure is shown in **Figure 9(b)**. The hydrogen content was reduced about 20% when the working pressure is increased from 1 to 19 Pa. The location of this mode experiences a slight shift to higher wavenumbers with working pressure, which implies an amorphous phase change. It is well known that an increase in the gas pressure enhances the collisions in the plasma and reduces the electron and ion energies, and hence decreases the crystallinity.

http://dx.doi.org/10.5772/63529

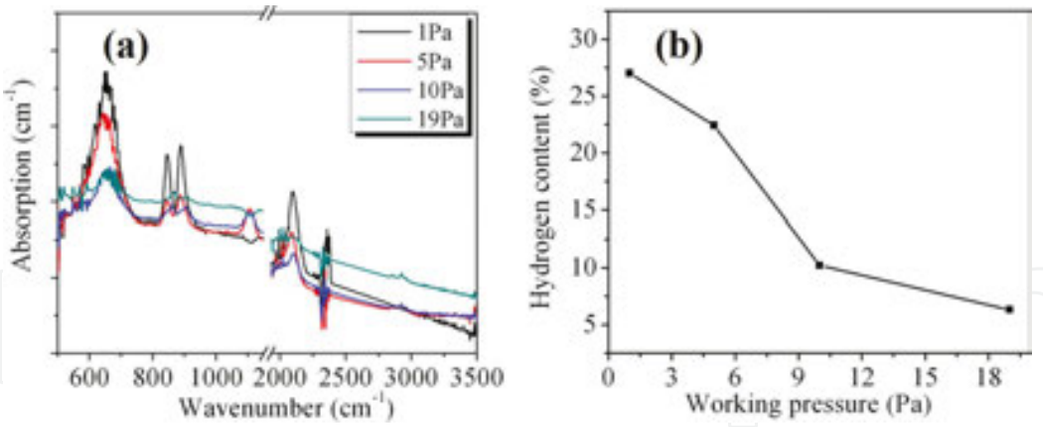

Figure 9. FTIR absorptance spectra of the a-Si:H thin films deposited at different pressures (a), and deduced hydrogen content C_H in the films (b).

It is worth noting that the stretching mode also decreases considerably with increasing working pressure. Assuming the stretching mode corresponds to SiH-associated peak at 2000 cm^{-1} and the SiH_2-associated peak at 2100 cm^{-1}, we will note the severe decrease of SiH_2 fraction in this mode. This should be responsible for the reduced hydrogen content in the a-Si:H films.

In summary, the working pressure substantially influences the optical band gap E_g and hydrogen content of the films. In present LFICP deposition, the high E_g values larger than 2 eV is mainly correlated to the high hydrogen content C_H which corresponds to the ultra-low working pressure.

2.7. Effect of substrate temperature

The substrate temperature substantially affects the plasma species diffusion on the surface and nucleation process, and hence the properties of the resulting a-/μc-Si:H thin films. In this set, the feed gas flow rate ratio is SiH_4/H_2 =5:20 (in sccm) and the discharge power is 2.0 kW. The substrate temperature is varied in the range of 27–150 °C. **Figure 10** shows the temperature-

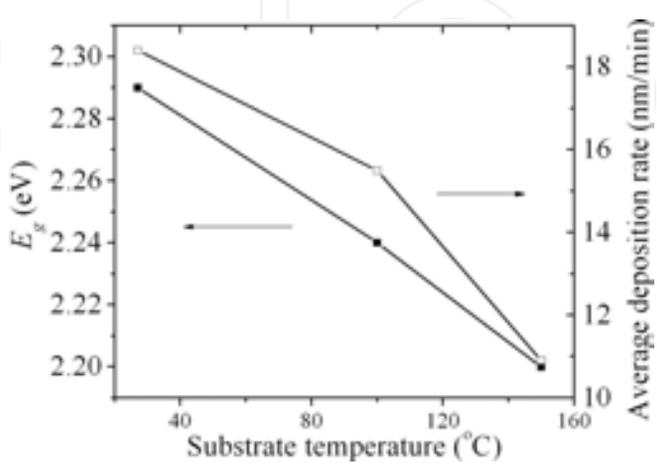

Figure 10. The substrate temperature-dependent deposition rate and E_g.

dependent deposition rate and E_g. The increasing substrate temperature leads to the decrease in both of these two parameters. In the studied temperature range, deposition rate and E_g decreases by about 7.5 nm/min and 0.9 eV, respectively.

Figure 11 shows the substrate temperature-dependent Raman spectra. The obtained films are highly crystalline under the present deposition conditions. The elevated substrate temperature results in the enhanced intensity of the 520 cm^{-1} peak, and thus more order structure in the films.

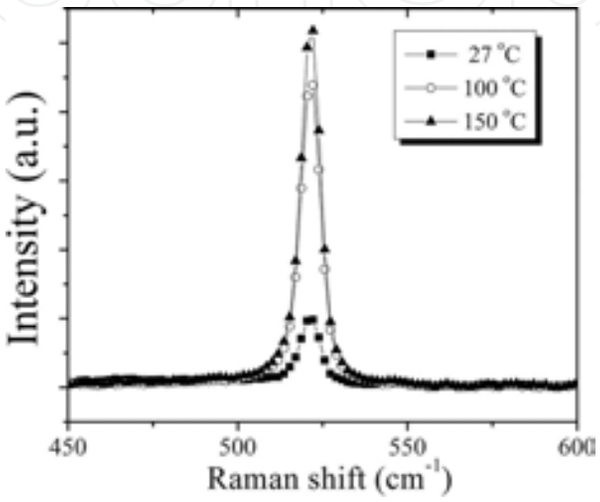

Figure 11. Substrate temperature-dependent Raman spectra.

The wagging/rocking mode in FTIR transmission spectra provides the bonded hydrogen numbers information which is displayed in **Figure 12**. The bonded hydrogen content C_H is very sensitive to the substrate temperature, decreasing by about 21% with substrate temperature from room temperature to 150 °C.

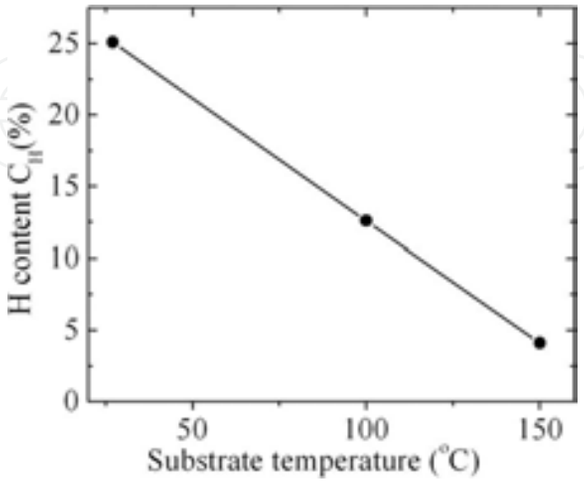

Figure 12. Substrate temperature-dependent hydrogen content in the films.

http://dx.doi.org/10.5772/63529

2.8. Effect of antenna-substrate distance

In the axial direction, the plasma properties should be dependent on the antenna-substrate distance *d* between the RF antenna and the depositing substrate. Although the detailed plasma characterizations in different distances have not been conducted, the different plasma densities, electron temperatures, and sheath potentials, etc. are expected. In principle, the neutral particles will become more and more important among species contributing to the film deposition due to the enhanced ion recombination with increasing distance *d*. It was recognized that the severe etching and ion bombardment produces additional defects on growing surface/substrate directly contacting with the high-density plasma [16]. Therefore, the deposition region should avoid direct contact with the high-density plasma during deposition. **Figure 13** shows the Raman spectra of the films deposited at different *d* values. The film is completely crystal in the case of direct plasma at *d* = 11 cm. In comparison, microcrystalline silicon is obtained when the distance is widened to 33 cm (namely, a semi-remote plasma configuration). The film is completely amorphous at the distance of *d* = 53 cm (a remote plasma configuration). Meanwhile, the atom network evolution from crystalline to amorphous is accompanied with the deposition rate reduction shown in **Figure 14**. The drastic reduction of deposition rate with distance *d* reflects the decreasing number of precursors contributing to Si:H deposition.

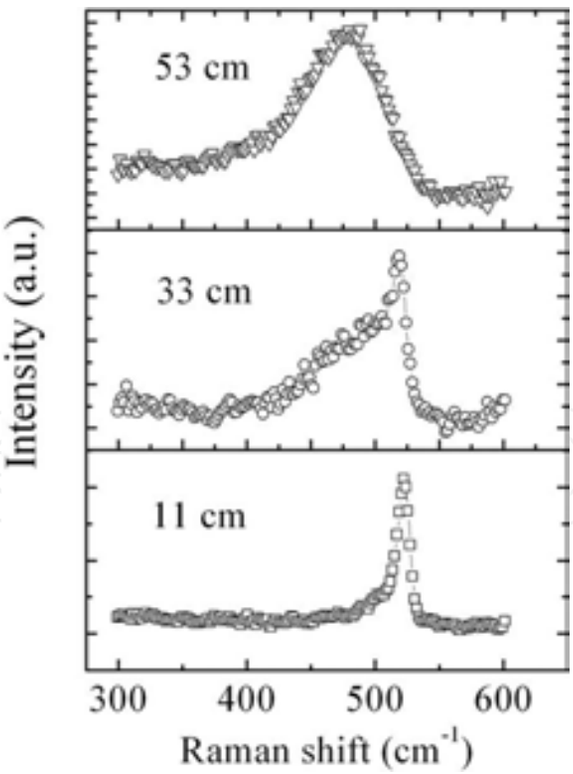

Figure 13. Raman scattering spectra of the silicon thin films deposited at different antenna-substrate distance *d* values. The other deposition parameters are as follows: discharge power 1.8 kW, substrate temperature 100 °C, and gas pressure of 7.2 Pa.

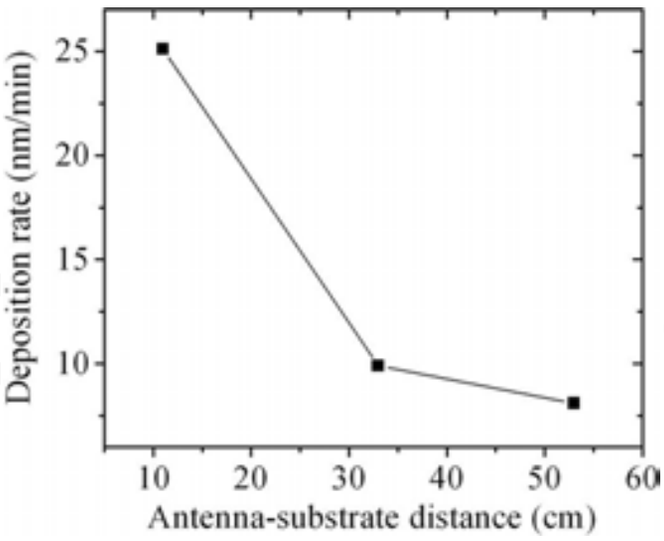

Figure 14. The antenna-substrate distance-dependent deposition rates.

Figure 15 shows the evolution of FTIR absorbance spectra with respect to the distance *d*. All the H-associated signals are enhanced with distance *d*. The hydrogen content C_H deduced from the wagging/rocking mode is represented in the inset. C_H increases sharply with *d* possibly due to the reduced plasma heating effect.

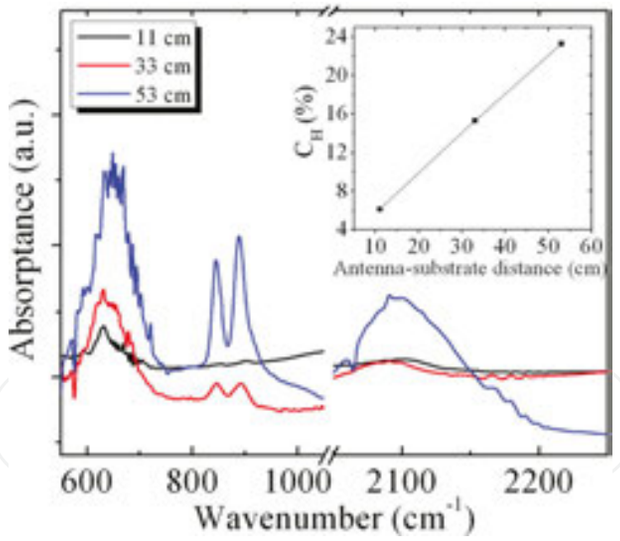

Figure 15. Comparison of FTIR absorbance spectra of the films deposited at different antenna-substrate distance values.

2.9. Doped a-/μc-Si:H films by LFICP CVD

In this section, the process parameters-dependent microstructure and electrical properties of the n- and p-doped a-/μc-Si:H films are studied to evaluate the doping ability of LFICP. Doping of a-Si:H by PECVD was first demonstrated by Spear and Le Comber in Ref. [43]. The disor-

http://dx.doi.org/10.5772/63529

dered structure of a-Si:H was supposed to allow the incorporation of dopant into the amorphous network, thus impeding the doping of the material. Subsequently, the underlying doping mechanism of a-Si:H was further clarified by Street [44]. Nevertheless, the doping efficiency of a-Si:H (<1%) as a disordered material is much lower than in crystalline silicon [45].

Here, the feed gas silane is pure without hydrogen pre-dilution. The n-type dopant resource gas phosphine (PH_3) and p-type dopant resource gas diborane (B_2H_6) both were H_2-diluted to a 15% concentration. In the following discussions, the gas consumptions are directly denoted as the nominal flow rate. It was found that the antenna-substrate distance *d* also significantly affects the doping capability of LFICP. As an example, **Figure 16** shows the hole carrier concentration evolution with respect to the parameter of *d* under the same other parameters: SiH_4:H_2:B_2H_6 = 5:20:0.4 (in sccm), discharge power 2.0 kW and low substrate temperatures of 150 or 100 °C. When *d* is increased from 11 to 53 cm, the hole concentration drops sharply spanning a wide range of 10^{19}–10^{14} cm^{-3}. The result at 100 °C is also included in the case of 33 cm. Recalling the Raman results at different *d* values (**Figure 13**), one will find that carrier density is inversely proportional to the crystallinity of the films. This is consistent with the fact that amorphous network is more difficult to dope. In the next section, it will be revealed that larger-distance-deposited a-Si:H films provide more effective surface passivation effect on silicon. Hence, doping and passivation ability for LFICP-grown a/-μc-Si seem to be a contradiction.

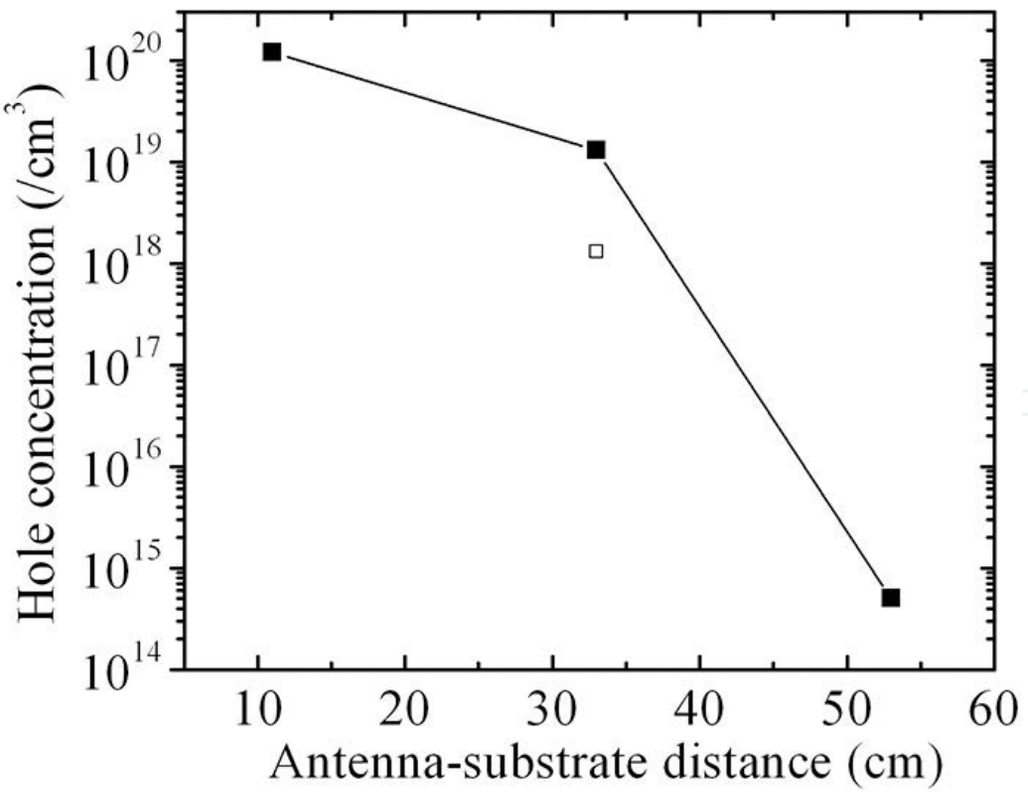

Figure 16. The hole carrier density as a function of antenna-substrate distance *d* in the p-doped films deposited at substrate temperature 150 °C (solid square) and 100 °C (open square).

2.9.1. p-doping

Different-flux phosphine gas was introduced into the feed gases of SiH_4:H_2 = 6:60 (in sccm) discharged by RF power of 3 kW with substrate temperature of 100 °C. **Figure 17(a)** shows the electrical parameters (from Hall effect measurement using the Ecopia HMS-3000 system) of as-deposited p-doped a-/μc-Si:H films. The hole density *p* reaches its maximum value of 1.2 × 10^{19} cm^3 at an intermediate B_2H_6 flux of 0.4 sccm. The ultimate conductivity *σ* displays the same trend with carrier density. The highest *σ* value is 0.58/Ωcm obtained at B_2H_6 flux of 0.4 sccm. The corresponding Raman scattering spectra of the films are shown in **Figure 17(b)**. A systematical shift from microcrystal to amorphous structure occurs with the gradual addition of dopant gas B_2H_6. The flux of 0.4 sccm is an optimum one, where the optimized amount of the dopant is introduced into the host μc-Si:H structures.

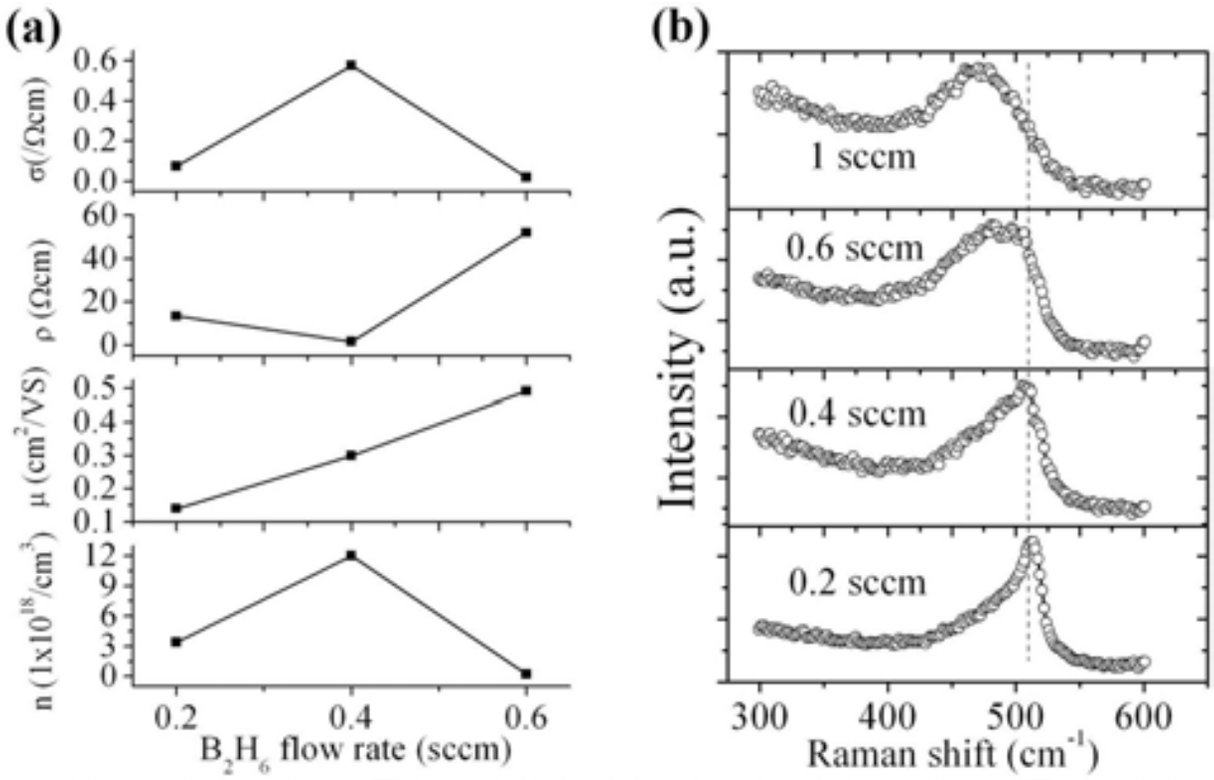

Figure 17. B_2H_6 flux-dependent electrical properties including the hole carrier density, mobility, resistivity, and conductivity (a), and corresponding Raman spectra of the a-/μc-Si:H films (b).

It is found that the doping is strongly dependent on the deposition temperature. Increasing substrate temperature improves the conductivity of the deposited films. **Figure 18(a)** shows the electrical properties of the doped a-/μc-Si:H films deposited in the substrate temperature range of 100–200 °C. The flux of B_2H_6 is kept at 0.4 sccm. The increased temperature facilitates the activation of the dopant in the film leading to the improvement in the hole density and degraded mobility. The resulting conductivity *σ* almost increases linearly with substrate

http://dx.doi.org/10.5772/63529

temperature and σ reaches 2.1/Ωcm. **Figure 18(b)** shows the corresponding Raman scattering spectra. The peak gradually shifts from 505 to 510 cm^{-1} indicating the microstructure shift to the microcrystalline side. This ordered network resulted from the higher substrate temperature is beneficial to doping behavior.

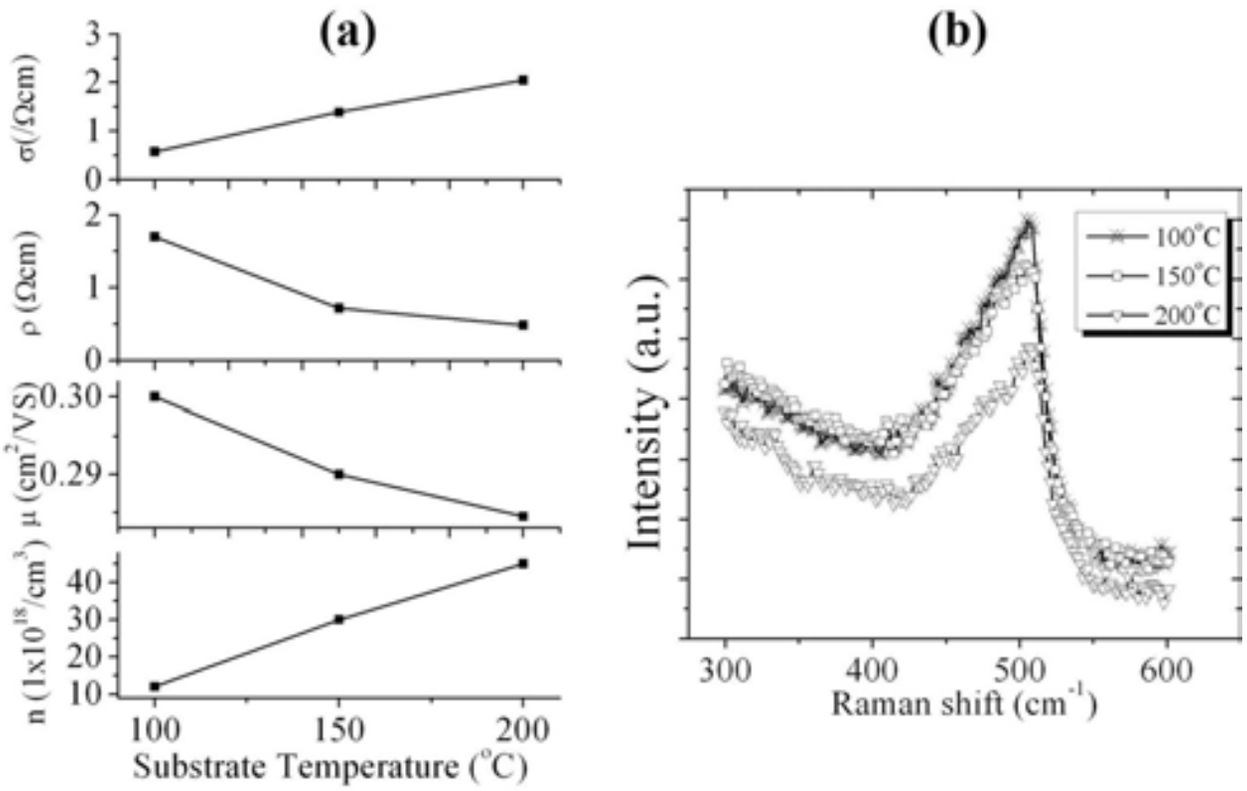

Figure 18. Electrical properties of the doped films with B_2H_6 = 0.4 sccm at different substrate temperatures (a), and the corresponding Raman scattering spectra (b).

2.9.2. n-doping

It seems that the n-doping is more difficult than p-doping in the case of higher antenna-substrate distance. Herein, the substrate temperature ranges from 100–200 °C, PH_3 flux covers the range of 0.5–1.0 sccm, and the feed gas ratio SiH_4:H_2 is changed from 5:40 to 5:60 (in sccm). The discharge power is set at 2.75 kW. **Figure 19** shows the Raman scattering spectra of the a-/μc-Si:H films n-doped by different PH_3 flux. The microstructure change with the PH_3 introduction is not as monotonic as shown in **Figure 17** associated with the case of B_2H_6. **Table 1** presents the deposition parameters and associated electrical properties of the obtained n-doped a-/μc-Si films. At PH_3 flux of 0.5 and 0.62 sccm (100 °C), the electron density n is below $10^{14}/cm^3$. The former flux 0.5 sccm is not adequate for effective doping and the latter 0.62 sccm leads to an amorphous-oriented network according to **Figure 19**. The optimum set is 0.75 sccm PH_3 and 200 °C, where the highest conductivity is 3.45/Ωcm.

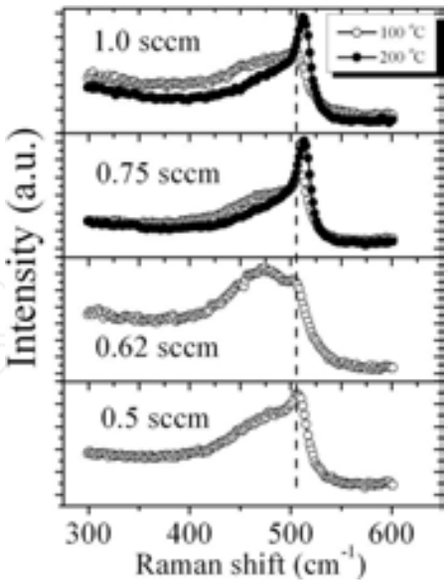

Figure 19. Raman scattering spectra of a-/μc-Si:H n-doped at different PH_3 fluxes.

Power	SiH_4	H_2	PH_3	Pressure	*T*	n	*μ*	*ρ*	*σ*
(kW)	(sccm)	(sccm)	(sccm)	(Pa)	(°C)	(/cm³)	(cm²/VS)	(Ωcm)	(/Ωcm)
2.75	5	60	0.5	12	100	4.11E+14	17.85	859	0.001
2.75	5	60	0.75	12	100	4.95E+15	6.34	199	0.005
2.75	5	60	0.75	12	200	1.03E+20	0.21	0.29	3.45
2.75	5	60	1	12	200	7.56E+19	0.031	2.68	0.38

Table 1. Deposition parameters and properties of n-doped a-/μc-Si:H thin films.

Figure 20 shows the n-doped a-/μc-Si:H films deposited with different hydrogen dilution ratio. Up to the ratio of SiH_4/H_2 = 5:50, the film is a completely amorphous network impeding the

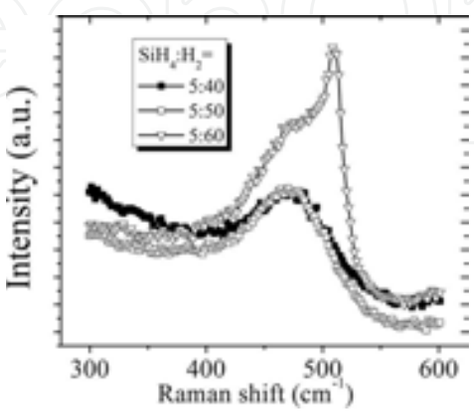

Figure 20. Raman scattering spectra of the n-doped a-/μc-Si:H films deposited at different hydrogen dilution ratio.

http://dx.doi.org/10.5772/63529

doping behavior. The structure turns into microcrystalline at the ratio of SiH_4/H_2 = 5:60, where the better conductivity can be obtained in present experiments.

Figure 21 shows a typical top view **(a)** and cross-sectional **(b)** SEM image of a n-doped μc-Si:H film deposited at a temperature of 200 °C and dilution ratio of H_2:SiH_4 = 60:5. Nanostructured Si particles are uniformly distributed on the surface in **Figure 21(a)**. There are no any observable voids or apparent defects. The apparent column growth is observed in **Figure 21(b)**. The interface between the film and the Si substrate is clear and free of incubation layer.

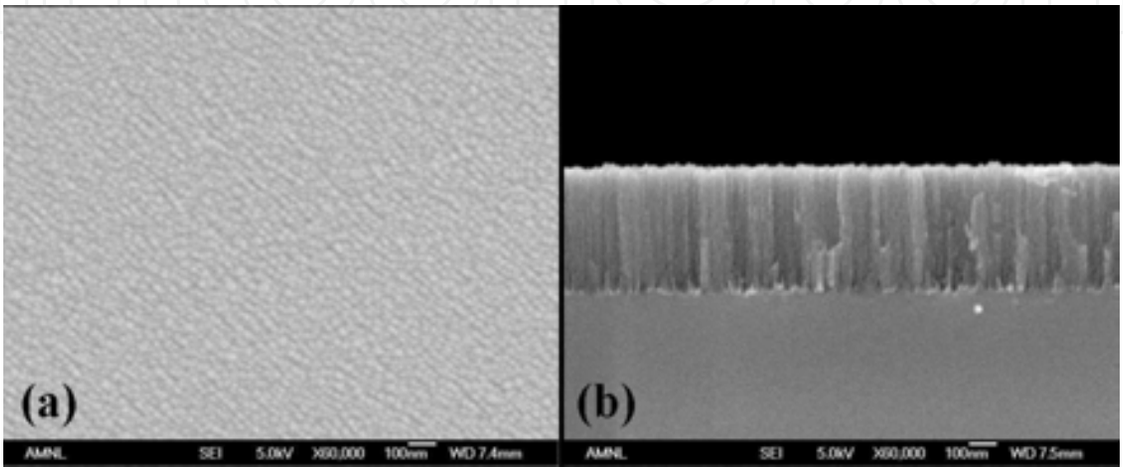

Figure 21. Top view (a) and cross-sectional SEM image of the n-doped μc-Si:H.

3. c-Si surface passivation by LFICP CVD a-/μc-Si:H

In Sections 1–2, the intrinsic and doped a-/μc-Si:H films based on LFICP-CVD method are studied in terms of the plasma parameters. The optical band gap, bond configuration, microstructure, and hydrogen content in the films are dependent on the deposition parameters of RF power, gas ratio, working pressure, and substrate temperature. In particular, the properties of the LFICP-grown a-/μc-Si:H films are sensitive to the antenna-substrate distance *d*. A high *d* value is inclined to a-Si:H over μc-Si:H growth due to avoiding direct immersion in high-density plasma. However, increasing *d* makes it difficult to dope the a-/μc-Si:H films. Improving substrate temperature and hydrogen dilution can effectively compensate the doping obstacle from increased *d*. The conductivity of 2.10 and 3.45/Ωcm are achieved in p- and n-doped μc-Si:H at a low substrate temperature of 200 °C.

In this section, the crystalline silicon surface passivation by LFICP-CVD a-/μc-Si:H is investigated. In terms of the antenna-substrate distance *d*, a-/μc-Si:H films display different passivation level evaluated by the carrier lifetime measurements. The passivation effect of the film, which is strongly dependent on a variety of processing conditions, e.g., the pre-deposition treatment of c-Si, the film deposition parameters, and post-deposition annealing, is physically analyzed. The carrier recombination mechanisms will be firstly reviewed.

3.1. Recombination and passivation in Si-based solar cells

Usually, the loss in photovoltaic solar cell comprises surface light loss, the transmitted light loss, thermalization loss (thermal electron loss). In a practical heterojunction (HJ) silicon solar cell, the a-/μc-Si:H layer is of several nanometers thick, which marginally absorbs sunlight. The photogeneration of excess charge carrier pairs mainly occur in the bulk c-Si. In order to efficiently collect the photogenerated carriers which can be extracted and thus contribute to the externally retrievable current, reducing the carrier recombination in silicon, especially on the surface, is particularly important.

The carrier recombination originating from bulk silicon primarily comprises two types, i.e., the intrinsic and extrinsic ones. The intrinsic recombination, which mainly includes radiative [46] and Auger recombination [47], occurs in a pure and defect-free semiconductor, while the extrinsic recombination stems from contaminants and defects which act as recombination centers.

Total bulk recombination is the sum of the above three terms and is expressed as

$$U = U_{Rad} + U_{Aug} + U_{SRH} = \frac{\Delta n}{\tau_{Rad}} + \frac{\Delta n}{\tau_{Aug}} + \frac{\Delta n}{\tau_{SRH}} = \frac{\Delta n}{\tau_b} \tag{4}$$

where τ_{SRH} denotes the contribution from the extrinsic recombination of Shock-Read-Hall effect [48, 49].

Surface recombination is a special case of SRH recombination due to the localized states appearing at the surface. Different from the bulk SRH centers, these states usually form a set of states across the band gap instead of a single energy level. Surface recombination is usually evaluated in terms of surface recombination velocity (SRV) instead of lifetime. However, the principles are same to bulk SRH recombination. It mainly originates from the surface dangling bond, i.e., the missing of crystalline network. The chemically and mechanically created defect can also result in surface recombination. In a simple condition with a constant bulk lifetime τ_b and a small constant SRV (two surfaces are same to each other), the effective lifetime τ_{eff} is expressed as

$$\frac{1}{\tau_{eff}} = \frac{1}{\tau_b} + \frac{2S_{eff}}{W}, \tag{5}$$

where W is the thickness of the bulk silicon.

High carrier lifetime is a critical issue in achieving high-energy conversion efficiency in solar cells. There are many techniques that have been developed over the past two decades with the objective of measuring minority carrier lifetime in Si [50]. Two techniques, namely the transient photoconductance decay (TPCD) and the more recent quasi-steady-state photoconductance

http://dx.doi.org/10.5772/63529

method (QSSPC), are the basis of the WCT-120 tester, which are widely used in this work to characterize the solar cell precursors.

Compared with the optical management by conventional methods like an antireflection layer, the minimization of electronic losses at the crystal silicon surface is a more delicate challenge for high-efficiency solar cell [51]. Recombination losses at silicon interface or surface can be minimized by using two passivation schemes, namely, via chemical passivation or filed passivation. The former aims to reduce the interface defects that originate from the dangling bonds by H atom, a thin dielectric, or semiconductor film. The latter is based on the fact that the electron/hole density at the interface will be significantly reduced by formation of a built-in potential from the introduction of a passivation layer. Based on these two strategies, various Si-based materials, such as hydrogenated amorphous silicon (a-Si:H) [52], silicon nitride (SiN) [53], thermal oxygenated silicon dioxide (SiO_2) [54], and amorphous silicon carbide (a-SiC_x) [55] have been investigated for passivation purposes. Among these materials, a-Si:H is still the best candidate for silicon heterojunction solar cells [56, 57] due to its excellent passivation properties obtained at low deposition temperatures, and also simple processing without the introduction of any atoms other than silicon and hydrogen.

The a-Si:H (including SiO_x, SiN_x and SiC_x) passivation layers were mainly deposited by using conventional CCP-PECVD or hot wire chemical vapor deposition (HWCVD) in literatures. A detailed review of c-Si surface passivation can be found in Refs. [2] and [51], where the millisecond level lifetime and below tens cm/s surface recombination velocity prevails. Schmidt et al. [59] used a-$Si_{1-x}N_x$ deposited at a temperature 300 °C ≤ T ≤ 400 °C and obtained recombination velocity S ≤ 10 cm/s. Martin et al. [60] adopted a-SiC_x:H as a c-Si surface passivation layer yielding S ≤ 30 cm/s. Dauwe et al. [61] achieved a low recombination velocities S ≤ 10 cm/s by 200–250 °C deposited a-Si:H. Descoeudres et al. [52] adopted a VHF-PECVD (40.68 MHz) to deposit intrinsic silicon film for c-Si surface passivation and obtained a lifetime of 5.9 ms in N-type FZ Si wafer with a resistivity of 4.0 Ωcm. Furthermore, the authors proposed a new indicator of silane depletion fraction for good passivation effect. It was reported that the good interface passivation corresponds to the highly depleted silane plasma. Willem et al. [2] prepared the a-Si:H film using three different CVD techniques, namely, PECVD, VHF-PECVD, and HWCVD for passivation purpose and found that all three deposition methods yield excellent surface passivation with milliseconds level lifetime values.

However, the ICP-grown a-Si:H for c-Si surface passivation is rarely reported [30], not to mention that grown by LFICP.

3.2. c-Si surface passivation by semi-remote LFICP CVD a-/μc-Si:H

It was found that a-/μc-Si films deposited at direct LFICP region (with an antenna-substrate distance d = 11 cm) had an unsatisfied passivation effect for c-Si due to the damaged interface by severe ion bombardment. Therefore, the distance must be lengthened in order to yield the high-quality interface and good passivation. In this subsection, the adopted distance is d = 33 cm, where a semi-remote plasma is obtained.

3.2.1. Passivation effect of a-/μc-Si:H deposited from hydrogen-diluted silane

In this subsection, a-/μc-Si:H films deposited from only hydrogen-diluted silane at the antenna-substrate distance of d = 33 cm is used to passivate c-Si surface with different resistivity. First, the surface passivation effect of a-/μc-Si:H grown under different discharge powers has been investigated in the case of a higher substrate resistivity of 8 Ωcm. The effect of pre-deposition hydrogen plasma treatment, post thermal annealing, and the correlation between the lifetime and the thickness of the incubation layer at the interface have been analyzed. At this antenna-substrate distance, the resulting films possess fairly good passivation even without any post-deposition thermal annealing.

The a-/μc-Si:H thin films of thickness of 50 nm were deposited on the double-side polished, p-type CZ Si (comparatively higher resistivity of 8 Ωcm, thickness of 600 μm, (100) orientation, and area of about 3 × 3 cm^2). The pre-deposition hydrogen plasma treatment on the substrates was applied for various durations to investigate the effect of hydrogen plasma exposure on the surface recombination. The microstructures and properties of the thicker counterpart of the thin passivation layer were studied in Section 2.1. The effective minority carrier lifetime of the symmetrically passivated wafer was measured by using the quasi-steady state photoconductance decay (QSSPCD) technique on the facility of WCT-120.

3.2.1.1. Effect of pre-deposition H_2 plasma treatment on surface passivation

Prior to the passivation layer deposition, the substrates were treated by H_2 plasma for different durations (0–90 s) to improve the interface properties. The final structure for the minority carrier lifetime measurement is shown in inset of **Figure 22**. All the specific minority carrier lifetimes were recorded at an excess carrier of $10^{15}/cm^3$.

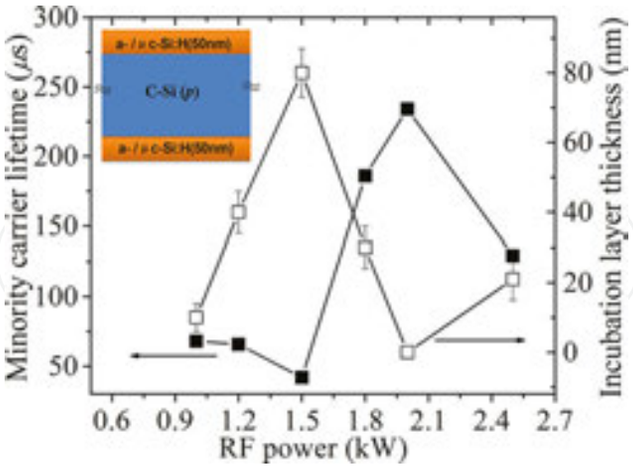

Figure 22. RF power-dependent minority carrier lifetime (filled squares) and incubation layer thickness (open squares). The inset shows the passivation scheme for the lifetime measurement.

τ_{eff} values are plotted in **Figure 23** as a function of H_2 plasma treatment time. τ_{eff} is 127 μs without H_2 plasma treatment. An intermediate treatment time (30–60 s) is beneficial to silicon surface passivation, which is evidenced by the improved lifetime value. However, overlong

http://dx.doi.org/10.5772/63529

treatment (>60 s) is detrimental to the surface quality, resulting in a less lifetime value of 73 μs. The maximum value of carrier lifetime ~230 μs was obtained at a time of 30 s.

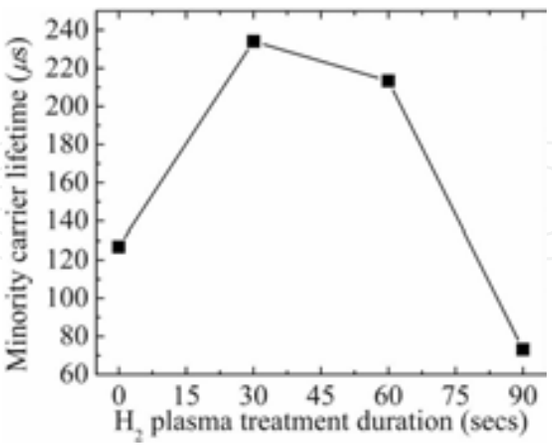

Figure 23. The minority carrier lifetime of the sample exposed to H_2 plasma for different time before the passivation layer deposition.

3.2.1.2. Influence of RF power on surface passivation

The RF power-dependent effective lifetime τ_{eff} is shown in **Figure 22** (filled squares). This curve can be separated into three stages: In the first stage (1.0–1.5 kW), τ_{eff} decreases from 67 to 42 μs; in the second stage (1.5–2.0 kW), τ_{eff} rapidly increases from 42 μs to its maximum of 234 μs; in the third stage (2.0–2.5 kW) τ_{eff} drops down to 129 μs. The observed pattern of τ_{eff} will be explained in terms of the properties of the thin films and the interface between the thin film and silicon substrate.

The passivation effect described by τ_{eff} is not only related to the deposited thin films itself but also the a-Si:H/c-Si interface quality. The low defect density in the thin films is presumably a consequence of hydrogen passivation. As mentioned above, the hydrogen content in these thin films is comparatively larger. However, in the current experiments, the maximum value of τ_{eff} is obtained at RF power of 2.0 kW, where the corresponding thin film contains the least hydrogen as shown in **Figure 5**. Therefore, the change of lifetime τ_{eff} should not simply be attributed to the change of hydrogen content with the RF power.

Another crucial mechanism to determine the passivation effect is the interface defect between the passivation layer and the substrate. It has been observed that during the deposition of a μc-Si:H layer on top of a substrate, a 30–50 nm thick interlayer referred as incubation zone [63] is produced. Its crystallinity and thickness strongly depend on the deposition condition and the substrate material. In our experiments, the incubation layer was directly observed in the high-magnification cross-sectional SEM images of the deposited thin films on double-side-polished Si substrate. **Figure 24** shows the high-magnification cross-sectional SEM images of the thin films deposited at the power of 1.2 (a), 1.5 (b), 1.8 (c) and 2.0 kW (d). The clear scratches and cracks come from the cross-section preparation process. Except the sample deposited at 2.0 kW, evident incubation layers were observed between the crystal Si and the films. Fur-

thermore, the thickness of the incubation layers can be determined from the SEM measurement tool by making measurement multiple times at different locations and the results as a function of RF power are plotted in **Figure 22** (the open squares). The error bars shown in **Figure 22** represent the standard deviations from the mean thickness values from the multiple metering. At a power of 1.5 kW, the thickness has a maximum of 80 ′ 7 nm (>the standard passivation layer thickness of 50 nm), while the lifetime has a minimum of 42 μs. No evident incubation layer was observed at the power of 2.0 kW, at which the greatest minority lifetime value was obtained. Linking the curve of incubation layer thickness with that of the lifetime, one will find that the incubation layer thickness changes with the RF power in an opposite way to the minority carrier lifetime τ_{eff} dose. This observation suggests the fact that the incubation layer on the interface between the passivation layer and the crystal Si will worsen the passivation effect of the a-/μc-Si:H thin films.

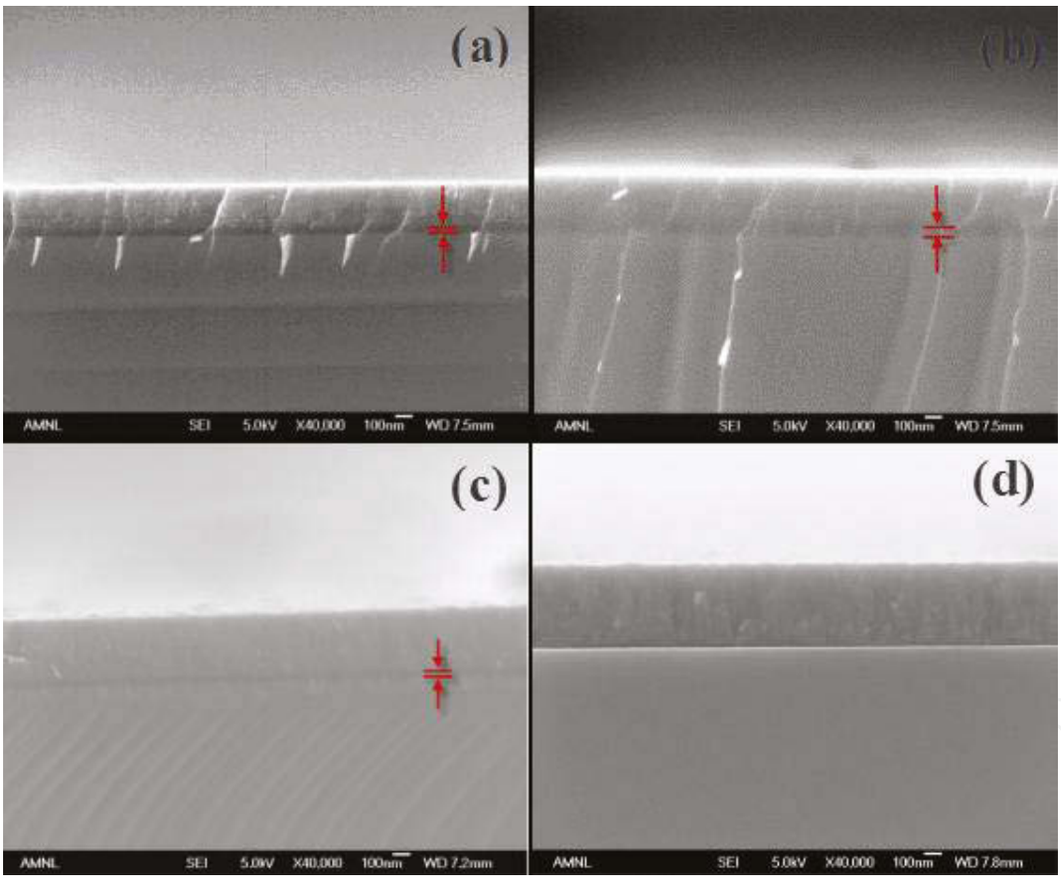

Figure 24. The cross-sectional SEM images of the thin films deposited at RF power of 1.2 (a), 1.5 (b), 1.8 (c), and 2.0 k W (d). Evident incubation layers were observed at the interfaces.

The CVD deposition of Si thin films involves a complex combination of several processes including the arrival and removal of gas molecules or precursors at the substrate surface, the decomposition into reactive species, and the migration of these species on the surface where they can lead to nucleation and continued deposition [64]. The adsorbed reactive species are likely to come to rest when a position of minimum energy position is found. The minimum

http://dx.doi.org/10.5772/63529

energy position can be a defect at the substrate surface, which will result in a new nucleus, or an existing nucleus [65]. At certain process conditions, the formation of nuclei will be delayed for some time known as the incubation time [64]. From the point view of the growth mechanism, the incubation layer (initial growth) will be rich of defects, which will lead to the intense recombination of the photon-induced carriers and thus a decreasing lifetime value observed in **Figure 22**.

3.2.1.3. Influence of thermal annealing on surface passivation

In order to investigate the influence of the post-deposition annealing on the silicon surface, the samples were thermally annealed in vacuum and H_2 flow atmosphere. For simplicity, one sample with an as-deposited lifetime value of 196 μs was annealed just in vacuum in the temperature range of 230–500 °C. **Figure 25(a)** shows the evolution of lifetime τ_{eff} with annealing temperatures. The annealing duration at each temperature point is 30 min. One can see that the lifetime increases almost linearly in the range of 230–420 °C. Further increasing of temperature to 500 °C results in a significant decrease in lifetime value. The relatively low temperature (<500 °C) annealing in vacuum leads to the lifetime improvement by a factor of about 2.5. The corresponding FTIR transmission spectra of the sample before and after thermal annealing were measured in the wavenumber range of 550–950 cm^{-1} to clarify the H role in the surface passivation. The spectra of the as-deposited and the 420 and 500 °C annealed samples are shown in **Figure 25(b)**. The Si-H wagging/rocking mode at about 630 cm^{-1} slightly changes with temperature increasing from 230 to 420 °C. In comparison, this mode considerably recedes when temperature is increased from 420 to 500 °C, which is indicative of lower hydrogen content after annealing. The mode around 850–900 cm^{-1} also becomes weak after annealing at a temperature of 420 and 500 °C.

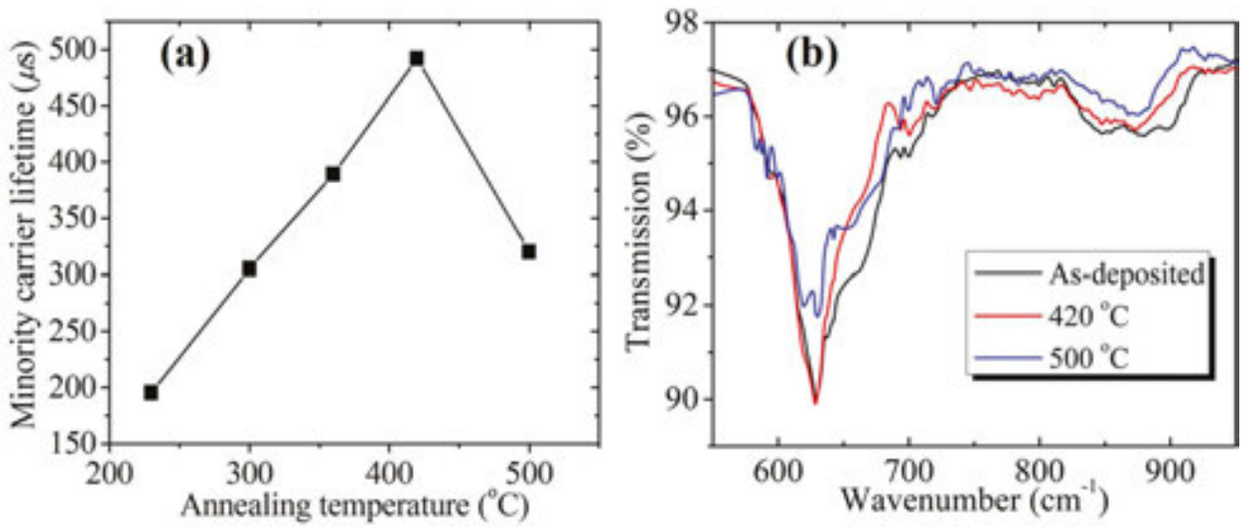

Figure 25. The minority carrier lifetime of the sample annealed at different temperatures in vacuum (a), and FTIR transmission spectra (550–950 cm^{-1}) of the as-deposited sample and that annealed at 420 and 500 °C (b). Increase in the annealing temperature from 420 to 500 °C leads to the decreasing hydrogen content in the film.

The vacuum annealing results discussed above represent the important role of the hydrogen atom in the Si surface passivation. Low-temperature (<420 °C) annealing enables the diffusion of hydrogen in the thin film towards the Si substrate, which effectively reduces the dangling bond density at the interface and enhances the minority carrier lifetime. At higher temperatures (>420 °C), hydrogen atom effuses leading to the re-generation of the dangling bonds and thus a decrease in the lifetime value. Systematic annealing experiments were performed on the samples deposited at different RF powers, and the ultimate lifetime values (not shown here) presented the same trend with that of the as-deposited samples shown in **Figure 22** (filled squares). These results show that the as-deposited interface features, especially the incubation layer properties discussed above, are the crucial factors in determining the ultimate lifetime values in our case. Therefore, we will focus on the sample with the highest as-deposited lifetime value. It is worth stressing that the ultimate lifetime value is dependent on the annealing circumstance. **Figure 26** exhibits the lifetime value evolution with annealing time at 420 °C in vacuum (filled squares), H_2 flow (filled circles), and N_2 flow. In the case of vacuum annealing, the lifetime value increases sharply in the 95 min and saturates at the value of 421 μs at about 185 min. On the contrary, the lifetime reaches the maximum of 524 μs in a short time of 11 min in the case of H_2 flow. It seems that the presence of hydrogen in the annealing circumstance is essential to improve surface passivation by present a-Si:H/μc-Si:H thin films, despite the presence of rich hydrogen in the film as evidenced by the FTIR result. With N_2 flow, lifetime reaches its maximum value of 425 μs in 5 min, followed by a drastic drop for time longer than 5 mins. The H_2 preference is confirmed by multiple annealing experiments. It is well known that N_2 is the commonly used protective gas for post-deposition annealing of passivation layer a-Si. But H_2 circumstance annealing is indeed better than N_2 in our experiments. The underlying mechanism needs a further study to clarify.

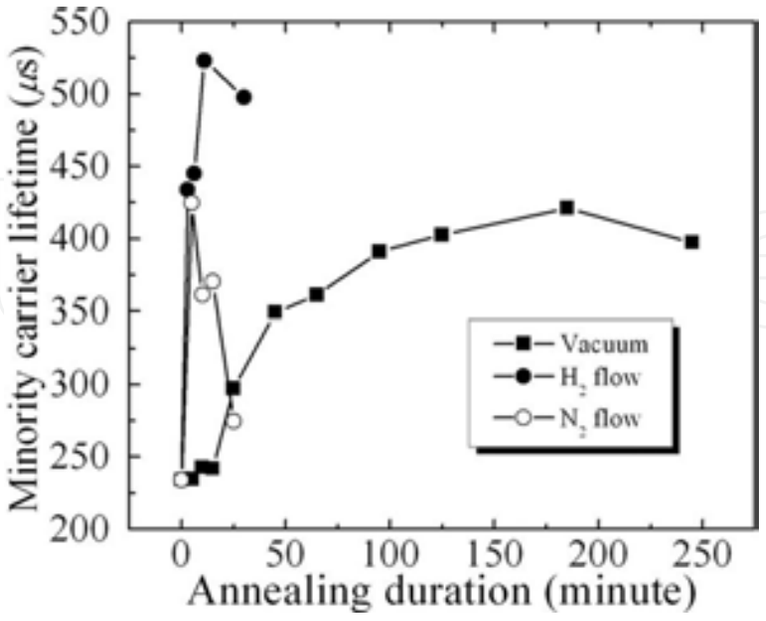

Figure 26. The minority carrier lifetime as a function of annealing duration at 420 °C at an atmosphere of vacuum (filled squares), H_2 flow (filled circles), and N_2 flow (open circles).

http://dx.doi.org/10.5772/63529

3.2.1.4. Injection level-dependent surface recombination

The effective minority carrier lifetime τ_{eff} is related to the effective surface recombination velocity S_{eff} through Equation 5. By neglecting the bulk lifetime ($\tau_b \rightarrow \infty$, we can get the maximum value of the surface velocity from this equation. The injection level-dependent S_{eff} with and without annealing is plotted in **Figure 27**. Comparing the results of the as-deposited and annealed, one can see that the low-temperature annealing leads to the decreasing of the surface recombination, especially in the range of the low injection levels. The as-deposited sample has a surface recombination of about 150 cm/s. The annealing at 230 °C for 11 min results in the decrease of S_{eff} above the injection level of 1 x 15/cm^3 and increase of S_{eff} below the same level. This abnormal increase in S_{eff} possibly stems from the excitation of the adsorbed atoms in the circumstance, which acts as the additional recombination centers to deteriorate passivation effect. Subsequent annealing at higher temperatures causes the continuous decreasing towards the injection level of 2.8 x 16/cm^3, where the Auger recombination plays a dominant role and the curves tend to converge. At the temperature of 420 °C, the lowest surface recombination velocity is 60 cm/s at the injection level of 1 x 15/cm^3. It should be emphasized that this S_{eff} value is the upper limit because of the adopting of an infinity assignment for the bulk lifetime.

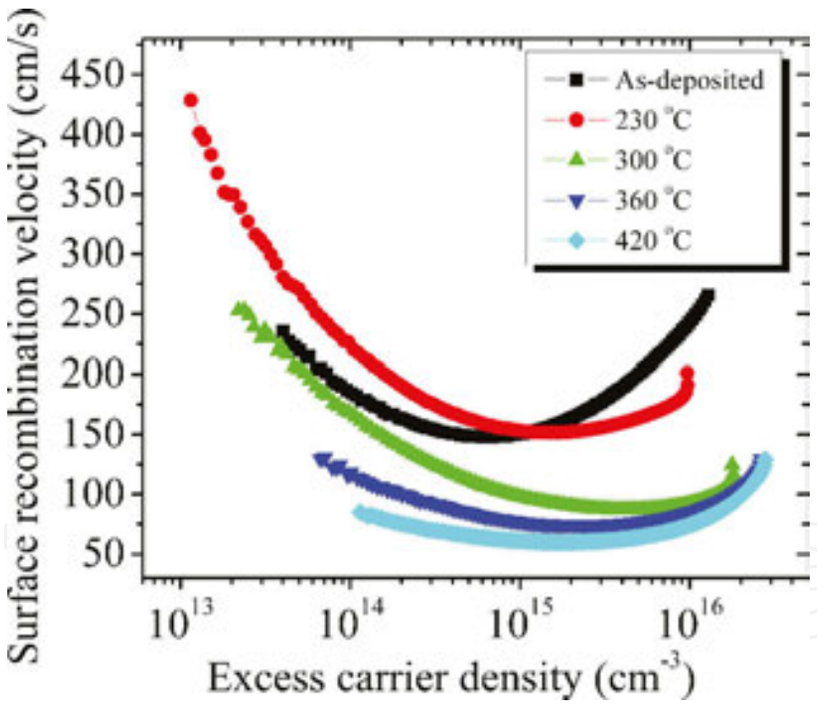

Figure 27. Injection level-dependent surface recombination velocity of the as-deposited sample and that annealed at different temperatures.

3.2.1.5. The high as-deposited lifetime values in the case of semi-remote LFICP

The present as-deposited lifetime value of 234 μs is much higher than that reported in literatures, where PECVD or HWCD methods were used to deposit the passivation a-/μc-Si-H layer. Jan-Willem et al. [62] summarized the passivation effects of a-Si:H deposited by

various methods: 34 μs for PECVD, 43 μs for VHF PECVD, and 87 μs for HWCVD. In principle, passivation can be physically divided into two types, i.e., hydrogen-related chemical passivation and built-in potential related field passivation. In the former, defect density can be remarkably lowered due to the reduced number of dangling bonds which is terminated by hydrogen atoms. With regard to the filed passivation, a-/μc-Si:H has a wider band gap than crystal silicon substrate, which results in a barrier on the interface preventing the recombination of photogenerated carrier pairs through the surface/interface defects.

It has been shown that the pre-deposition hydrogen plasma exposure significantly influences the surface passivation (see **Figure 23**). In the post-deposition annealing, the interaction between hydrogen atom from the passivation layer and the c-Si substrate is crucial to the surface passivation. Mitchell et al. [66] studied the thermal activation of the hydrogen-related chemical passivation on silicon substrate and determined the thermal activation energy of E_A through the following formula:

$$1/\tau_{reac} = A\exp(-E_A/k_BT) \tag{6}$$

where τ_{reac} is the reaction time between hydrogen atoms and silicon atoms, E_A the activation energy of surface passivation, k_B the Boltzmann constant, and T the temperature. According to Equation (6), a low E_A value will point to a high reaction rate $1/\tau_{reac}$ or a short reaction time τ_{reac}. In earlier works [33, 39], we analyzed the effect of high-density hydrogen plasma on the crystallization mechanism of LFICP-grown μc-Si:H. Abundant atomic hydrogen resulting from the dissociation of SiH_4 and H_2 will result in high surface coverage by hydrogen, which reduces the activation energy E_A and the reaction time τ_{reac}. In addition, high-density excited hydrogen atoms will recombine with the precursor of Si-H in the way described by the reaction H + Si-H→Si- + H_2 (with the dangling bond Si-). This recombination process can produce effective local plasma heating on the growing surface, which will contribute to the hydrogen atom transport to the interface and bulk silicon and a considerable lifetime value even without any additional thermal annealing.

3.2.1.6. Incubation layer and its thickness control

Figure 28(a) [**(b)**] shows a low- (high-) magnification cross-sectional TEM micrograph of LFICP-grown μc-Si:H on silicon substrate. In **Figure 28(a)**, a clear incubation layer (dark area) between the film and substrate is discriminated like in SEM images. **Figure 28(b)** exhibits more details of the interface. The grey area in the film corresponds to the microcrystalline Si fractions, which are conical conglomerates of microcrystals. As observed above, the incubation layer is detrimental for the improvement of lifetime and its thickness is highly dependent on the process parameters, e.g., the applied RF power in present experiments. Therefore, a deep understanding on the mechanism to control the formation of incubation layer is extremely important. It was recognized that the ion bombardment played a crucial role in the formation of incubation layer [67]. The ion beam works in two possible ways, namely (i) a surface effect: very small grains do not survive the high dose of ion irradiation, thereby reducing the nucleation rate, (ii) a bulk effect: the ion beam induces defect-related grains growth. Accord-

http://dx.doi.org/10.5772/63529

ingly, two strategies [67] to control the ion beam were proposed: the choice of the frequency of the power source generating the plasma, and the design of the electrode configuration to avoid its formation. In present antenna-substrate distance d = 33 cm, most of the ions/electrons energy is around several eVs, below the threshold value of 16 eV for defect formation for Si. Therefore, the lengthened distance d makes it possible to minimize the effect of the ion bombardment to an acceptable level.

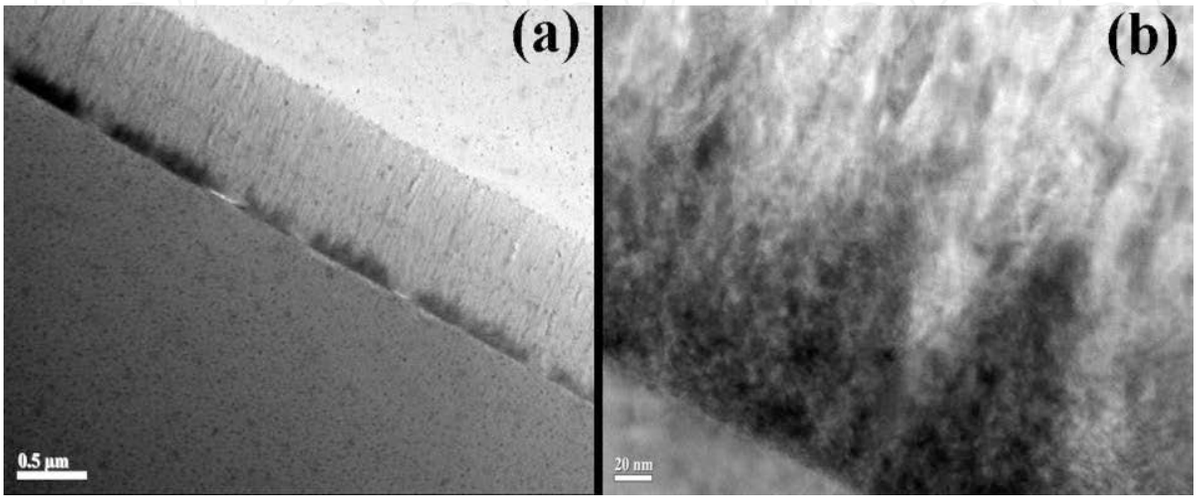

Figure 28. A typical cross-sectional TEM micrograph of LFICP-grown μc-Si:H films on Si substrate at low (a) and high (b) magnification.

From the point of view of a growth mechanism, the key to diminish the initial growth of incubation layer seems to be the rapid nucleation without retard on the interface. In present experiment, this occurs at the power of 2.0 kW, near the transition point (1.8 kW) from a-Si:H to μc-Si:H. This is consistent with some authors' findings that the good passivation effect is obtained with microcrystalline-oriented passivation layers, where the depletion fraction of SiH_4 is comparatively higher than that of amorphous regimes [52, 68]. In the current study, although the silane depletion was not experimentally measured at certain RF power, the high depletion fraction at the power of 2.0 kW is expected. The detailed relation between the depletion fraction and the incubation time in the growth of a-/μc-Si:H needs to be further clarified.

3.2.1.7. Passivation of low resistivity c-Si

It is more difficult to passivate a lower-resistivity Si surface due to the defect associated with more recombination. However, the lower-resistivity wafer is more meaningful in practical solar cell application. In this part, two types of wafers have been investigated: p-type (100), 2 Ωcm, and n-type (100), 3 Ωcm wafers. The process parameters such as discharge power, substrate temperature, dilution ratio, and post-deposition annealing have been widely explored to improve their surface passivation. **Figure 29** shows the effective minority carrier lifetime τ_{eff} in the n-type 3 Ωcm c-Si passivated with a-Si:H deposited at different substrate temperatures. τ_{eff} drastically drops from 164 μs to 25 μs with increasing substrate temperature

from room temperature to 140 °C. This is possibly originated from the local epitaxial growth or reduced hydrogen content with increasing temperature.

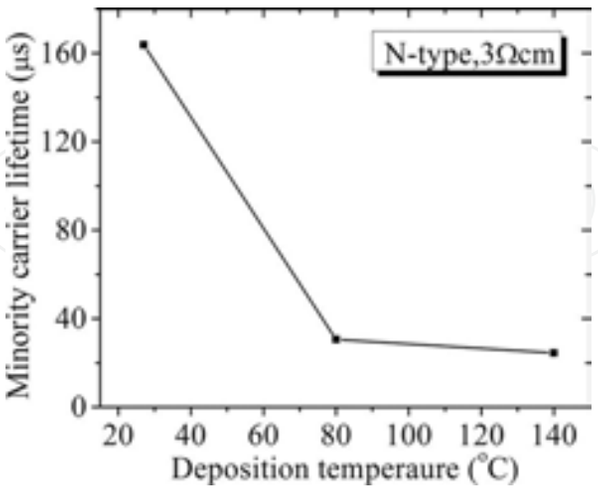

Figure 29. As-deposited lifetime values as a function of the substrate temperature. The other parameters are: SiH_4:H_2 = 12.5:12.5 (in sccm), discharge power 1.5 kW.

Figure 30 displays τ_{eff} in both types c-Si passivated by a-Si:H deposited from hydrogen-diluted silane with different dilution ratios (H_2/SiH_4). The discharge power and substrate temperature were kept at 2.0 kW and room temperature, respectively. The flow rate of SiH_4 and H_2 is 20:0, 12.5:12.5, 8.3:16.7, 5:20, corresponding to the hydrogen dilution ratio of 0, 1, 2, and 4, respectively. τ_{eff} reaches its maximum values at the dilution ratio of 1 in both p- and n-type c-Si. Based on the above analysis on passivation, the higher depletion of silane and reduced incubation layer are expected. **Figure 31** shows the discharge power-dependent lifetime values, which reached its maximum at RF power of 2.5 kW. Above 2.5 kW, τ_{eff} begins to drop again.

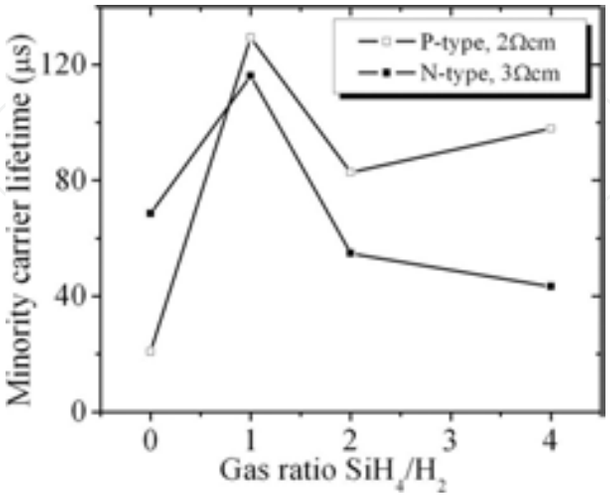

Figure 30. As-deposited lifetime values in both type c-Si passivated by a-Si:H grown from hydrogen-diluted silane with different dilution ratios.

http://dx.doi.org/10.5772/63529

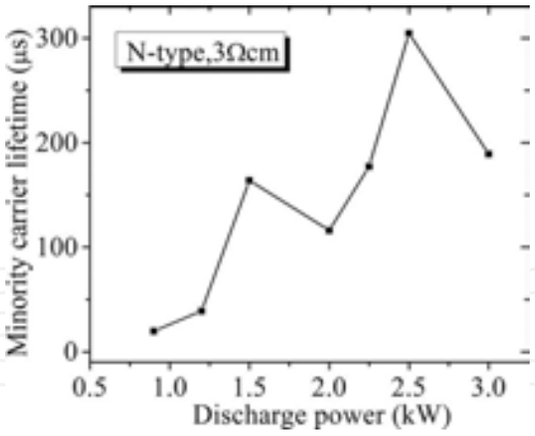

Figure 31. As-deposited lifetime values in N-type 3 Ωcm c-Si passivated by a-Si:H grown under different RF powers.

The optimized lifetime results of these two types of low-resistivity c-Si have been shown in **Figure 32**. At the specific excess carrier density of $10^{15}/cm^3$, the lifetime value is 305 and 150 μs for the n-type 3 Ωcm and p-type 2 Ωcm c-Si, respectively. It should be noted that these results are as-deposited values without post-deposition annealing. Unfortunately, post-deposition annealing cannot improve the lifetime values anymore in the present low-resistivity c-Si substrates. The hydrogen chemical annealing mentioned above has already raised the lifetime values to its maximum during the deposition process.

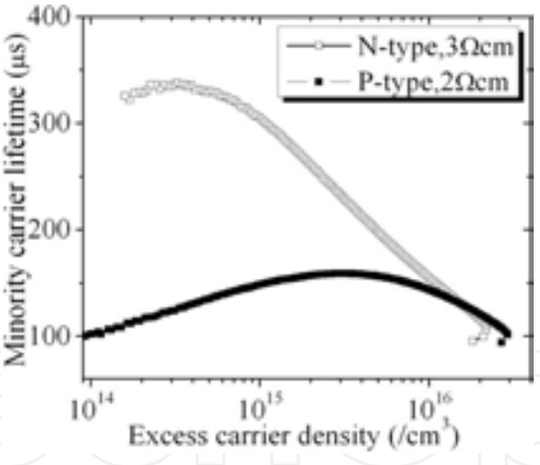

Figure 32. Injection level-dependent minority carrier lifetime in two types of low-resistivity c-Si wafers: p-type, 2 Ωcm and n-type, 3 Ωcm.

Although the as-deposited values without post-deposition long time annealing are much bigger than that reported in references, the present lifetime values are still lower than the ms level results in the literatures. The plasma density in the growth region has already been reduced a lot by increasing the antenna-substrate distance *d* to 33 cm. The semi-remote LFICP grown a-/μc-Si provides a very high as-deposited lifetime value in c-Si (low and high resistivity). In turn, these high as-deposited lifetime values reflect the still high-density plasma in the present growth area, which provides effective chemical annealing during the growth

process. On the other hand, the high-density plasma makes the growth surface exposed to a pronounced ion bombardment, which will damage the interface between the substrate and the passivation layer. In terms of process parameters, the high-discharge power points to the high silane depletion. Meanwhile, the ion bombardment on the substrate is inevitably enhanced under the increasing discharge power. In this sense, the key to improve the passivation effect lies in how to balance the silane depletion and ion bombardment on the interface.

3.2.2. Introduction of CO_2 into the reactive gas

a-Si:H is easy for (partially) epitaxial growth on c-Si even at low deposition temperatures, which will severely reduce the carrier lifetime values and thus the photovoltaic performance of HJ solar cell [56]. Incorporation of O into the amorphous silicon network can effectively suppress the epitaxial growth [69]. In the aspect of optics, the inherent blue light loss in a-Si:H layer also restricts the solar cell optimization. As a consequence, wide-banded Si-based materials become a promising candidate. Thermally grown SiO_2 provides a state-of-art level of surface passivation with a reduced surface recombination velocity as low as 2 cm/s [54]. However, the thermally grown SiO_2 suffers from the inherent disadvantages such as extremely high process temperature ((1000 °C) and low deposition rate. As a consequence, non-stoichiometric silicon oxide (SiO_x) based on non-thermal deposition methods have been proposed as an alternative to SiO_2. Apart from conventional PECVD and ESR, VHF-PECVD (13.56–110 MHz) has also been used to grow SiO_x:H for c-Si passivation [70, 71]. Mueller et al. [71] investigated the RF frequency effect on the passivation behavior for n-type FZ silicon wafer (resistivity (0.5 Ωcm) and obtained the minority carrier lifetime of 480 μs at the optimum frequency of 70 MHz. Hydrogen-diluted SiH_4 acts as the feedstock gas, whereas the oxygen source varies from oxygen gas [72] to various composites such us N_2O [73] and CO_2 [74].

In this section, CO_2 is introduced into the reactive gases of SiH_4+H_2 and efficiently dissociated in the LFICP system. The discharge power is set at 1.8 kW, flow rate of both SiH_4 and H_2 are 12.5 sccm, and no external heating is applied to the substrate. Various flow rates of CO_2 are introduced into the deposition chamber. The microstructure evolution with the introduction of CO_2 in the obtained films is investigated. Two types of c-Si wafers: n-type, 3 Ωcm and p-type, 2 Ωcm, are passivated by these films. The underlying passivation mechanism is analyzed.

Figure 33 shows E_g and deposition rate as functions of CO_2 flow rate. The incorporation of CO_2 into the reactive gases results in the effective widening of band gap E_g and the pronounced decrease in the deposition rate. E_g increases by about 0.3 eV with CO_2 increased from 0 to 12.5 sccm. According to Watanabe [75], SiO:H is a two-phase material with an island of SiO in a matrix of a-Si:H. In their two-phase model, the oxygen-rich phase is effective in increasing E_g and the Si-rich phase contributes to high conductivity. The widened E_g is beneficial to the light transmittance through the window layer when SiO_x:H is used as the window layer. Actually, Sritharathikhun et al. has succeeded in fabricating SiO_x:H HIT solar cell on n-type [76] and p-type [77] silicon substrate and obtained the competitive photovoltaic performance efficiency of 17.9% for n-type substrate, and 15.3% for p-type substrate.

http://dx.doi.org/10.5772/63529

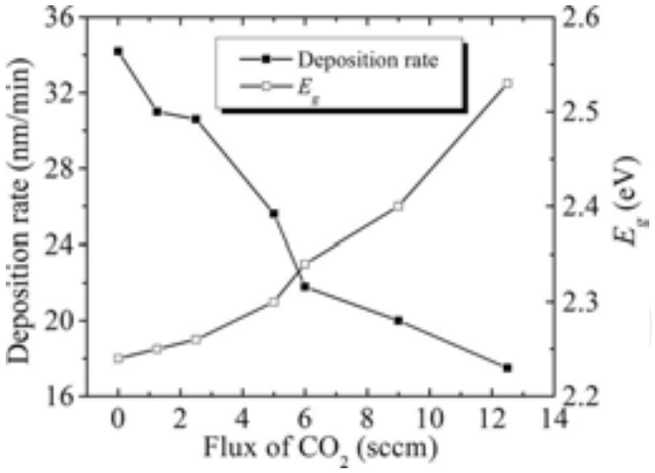

Figure 33. Deposition rate and optical band gap E_g evolution with CO_2 flow rate.

Figure 34 shows the FTIR absorbance spectra of the corresponding films. Besides the Si-H waging/rocking signal ((640 cm^{-1}) and Si-H stretching signal ((2100 cm^{-1}) usually observed in a-Si:H, some oxygen and carbon-associated modes appear. The Si-C stretching mode, which couples with the doublet signal of $(SiH_2)_x$ ((845–890 cm^{-1}) in the case of low CO_2 flow rate, grows stronger, and eventually dominates the latter. The Si-O-Si stretching mode located around 1100 cm^{-1} gradually shifts from 1107 to 1120 cm^{-1}. The former and latter are assigned to the nature of SiO_2 and SiO_x, respectively [78]. At minor CO_2 addition, the distinct peak at 1107 cm^{-1} is possibly due to the remaining oxygen in the deposition chamber. The consecutive increase of CO_2 makes the structure change from SiO_2 to SiO_x. Another effect of CO_2 addition is the shift of the Si-H stretching signal, indicating the incorporation of O into the Si-H bond. In literatures, carbon was regarded as being excluded because of the formation of volatile CO. However, the FTIR method tracks carbon in the form of Si-C bond in our experiment. Therefore, the obtained films can be strictly denoted as $SiC_{1-x}O_x$:H.

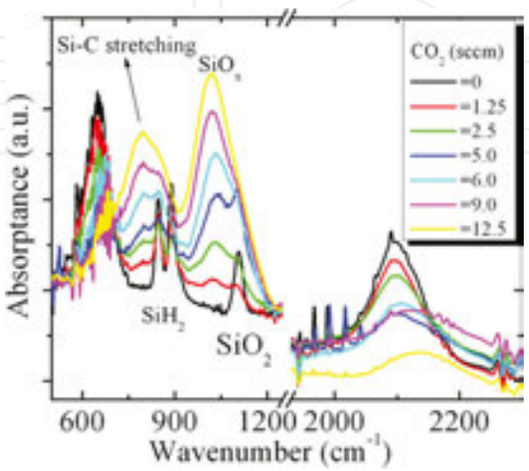

Figure 34. FTIR absorptance spectra of the deposited films with varying CO_2 flow rates.

About 60 nm thick $SiC_{1-x}O_x$:H films were deposited on both sides of the two types of c-Si substrate and the surface passivation was examined by the method of steady-state photoconductance decay method described above. **Figure 35** shows the effective lifetime values of these two substrates passivated by the $SiC_{1-x}O_x$:H films deposited with different flux of CO_2. At first glance, τ_{eff} degrades with the increasing addition of CO_2. This should be correlated to the increasing defect from the introduction of C and O into the network. However, incorporation of minor CO_2 is beneficial to the surface passivation. As an example, lifetime τ_{eff} has a highest value at flux of 2.5 sccm (1.25 sccm) in n-type (p-type) c-Si. The optimized injection level-dependent lifetime values before and after thermal annealing (275 °C, 30 min) have been presented in **Figure 36**. The obtained best results for n-type 3 Ωcm and p-type 2Ωcm are 313 and 166 μs at the specific carrier density of $10^{15}/cm^3$, respectively.

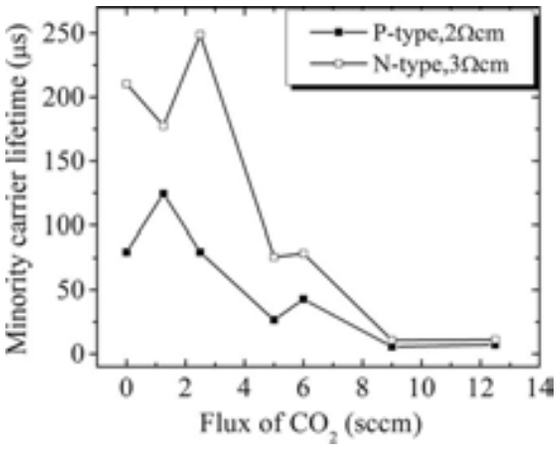

Figure 35. The as-deposited lifetime values in two types of c-Si substrates passivated by $SiC_{1-x}O_x$:H deposited with different flux of CO_2. The lifetime values are taken at the specific excess carrier density of $10^{15}/cm^3$.

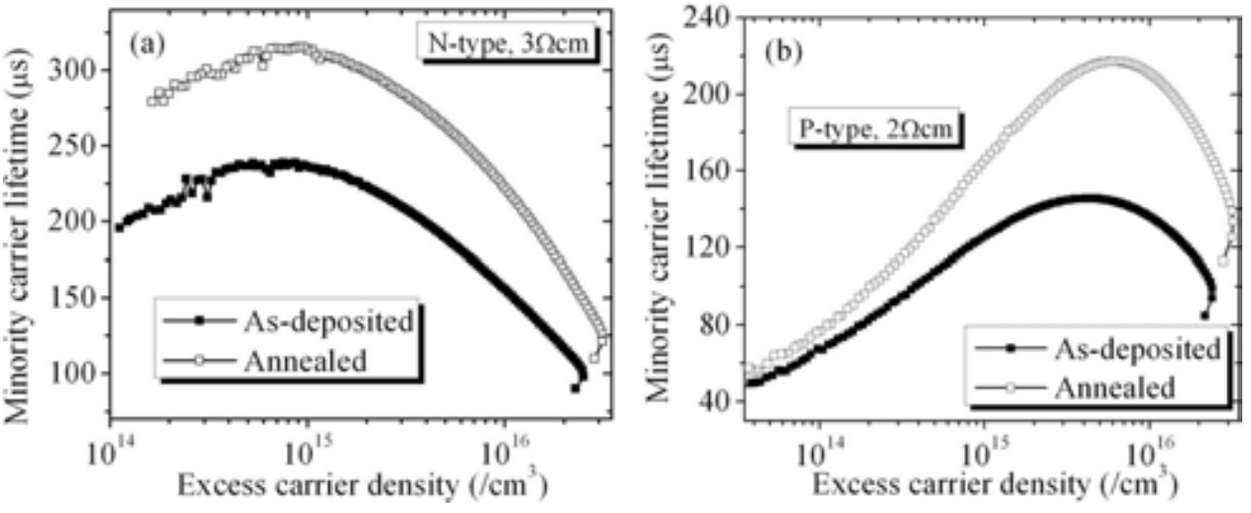

Figure 36. Injection level-dependent lifetime values in the substrate of n-type 3 Ωcm (a) and p-type 2 Ωcm (b) before and after the thermal annealing. The fluxes of CO_2 are 2.5 and 1.25 sccm in (a) and (b), respectively.

http://dx.doi.org/10.5772/63529

In order to clarify the passivation mechanism for the LFICP-grown $SiC_{1-x}O_x$:H, high-frequency (1MHz) C-V measurements were performed on a metal-semiconductor-insulator (MIS) structure shown in the inset of **Figure 37**. The insulator layer is $SiC_{1-x}O_x$:H material. The front contact is a small Al dot with a diameter about 0.5 mm and the rear contact is sheet Al. Al electrode was deposited by the method of magnetron sputtering. The amplitude of the AC signal was 10 mV. The work function difference of Al and silicon was kept at −0.85 V [79]. The recorded C-V curve is shown in **Figure 37**, from which a fixed charge density of $-2.7\times10^{11}/cm^2$ was deduced. However, this level is not high enough to contribute to the field passivation, which is usually accompanied by a fixed charge density of the order of $10^{12}/cm^2$ [74]. Therefore, the passivation effect of the present $SiC_{1-x}O_x$:H mainly stems from the chemical passivation like in a-Si:H case.

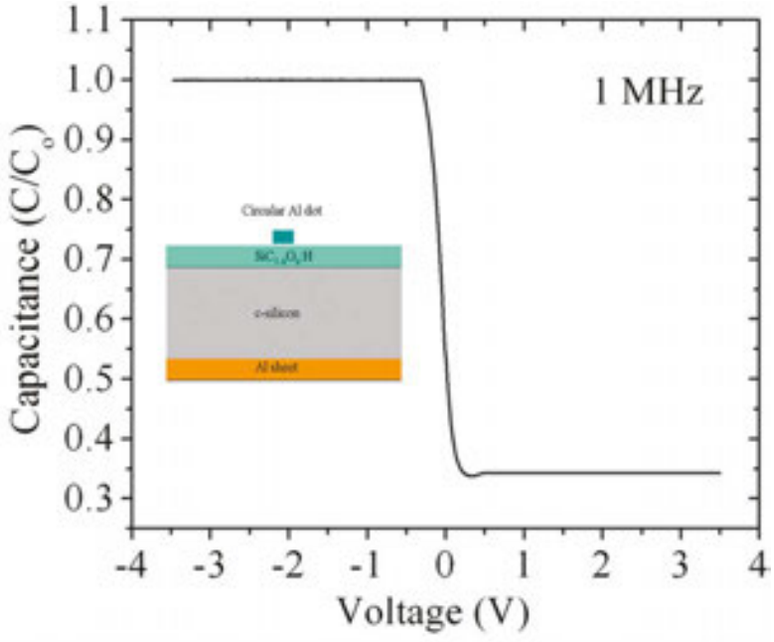

Figure 37. The C-V curve of the metal-semiconductor-insulator (MIS) structure, from which the fixed charge in the insulator can be deduced.

3.3. c-Si surface passivation by remote LFICP CVD a-Si:H

In subsection 3.2.2, reactive gas CO_2 was introduced into SiH_4+H_2 to improve the c-Si surface passivation. The introduction of CO_2 can widen the optical band gap of the passivation layer, and simultaneously suppress the partial epitaxial growth of the passivation layer on c-Si. The passivated sample exhibits high as-deposited lifetime values, whereas the lifetime values cannot be enhanced effectively after post-deposition annealing. It is believed that the frequent ion bombardment from the high-density plasma should be responsible for these two effects: it conveys energy to the growing surface acting as plasma annealing, and possibly results in damages to the interface. The damaged interface will define the hydrogen diffusion to the interface when annealing and results in a limited enhancement in lifetime. One possible

solution is to keep the substrate away from the plasma generation space. In this section, the antenna-substrate distance *d* is further enlarged to *d* = 53 cm to form remote plasma, and thus further decrease the ion bombardment on the surface.

Figure 38 shows the lifetime τ_{eff} curves before and after the thermal annealing in 275 °C for different durations. In **Figure 38(a)**, the as-deposited τ_{eff} value is 3 μs, and τ_{eff} surges upon annealing. The similar behavior is observed in the case of the n-type 4 Ωcm c-Si. The saturation values of 295 and 716 μs are achieved in p-type 1 Ωcm and p-type 4 Ωcm c-Si, respectively. The lifetime values τ_{eff} reaches their maximums at annealing duration of 45 min. The present annealing behavior is different from that in the case of antenna-substrate distance *d* = 33 cm. Herein, τ_{eff} is improved by more than two orders of magnitude after thermal annealing. This fact supports the assumption of the ion bombardment effect accompanying with a lower distance *d* value.

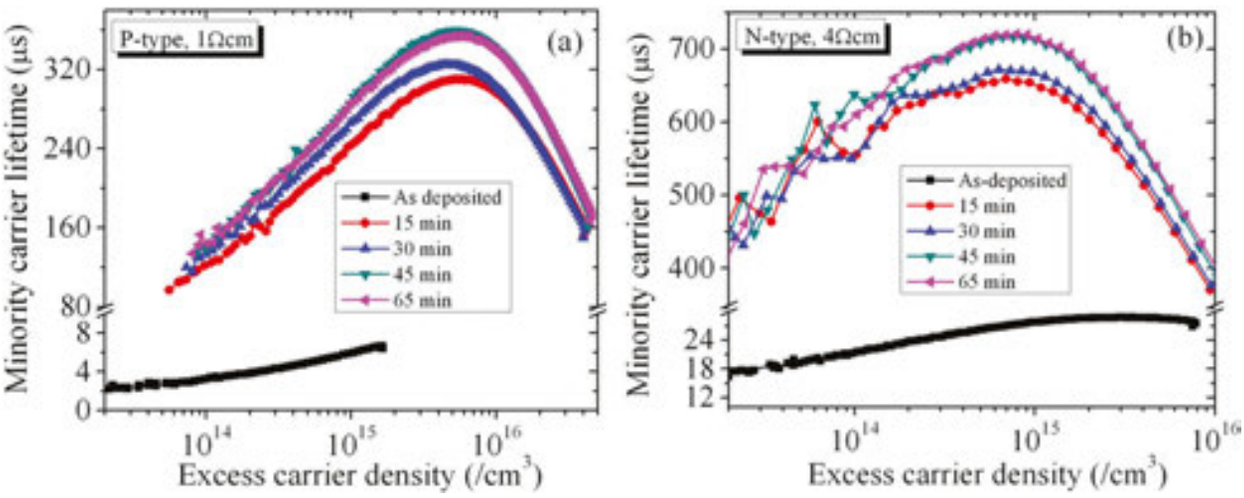

Figure 38. Injection level-dependent lifetime values in the p-type 1 Ωcm (a) and n-type 3 Ω cm (b) c-Si, before and after the thermal annealing. The thermal annealing was conducted at 275 °C in N_2 atmosphere for different durations.

In a narrow tunable working pressure range, we have compared the lifetime curve of the passivated samples under different pressures. **Figure 39** shows the comparison between the two discharge pressures of 0.2 and 1.0 Pa. The lifetime values are measured in the passivated c-Si substrates (n-type 4 Ωcm) before and after the thermal annealing treatment. The as-deposited lifetime values at 0.2 Pa are much greater than that at 1.0 Pa. Nevertheless, the vice verse is true after the thermal annealing. As mentioned above, a higher pressure means a smaller mean free path of the particles and a higher deposition rate. A faster growth can minimize the partial epitaxial growth of a-Si:H on c-Si surface. In addition, the lower-pressure mode possibly still causes some surface defects which limit the beneficial effect of thermal annealing.

http://dx.doi.org/10.5772/63529

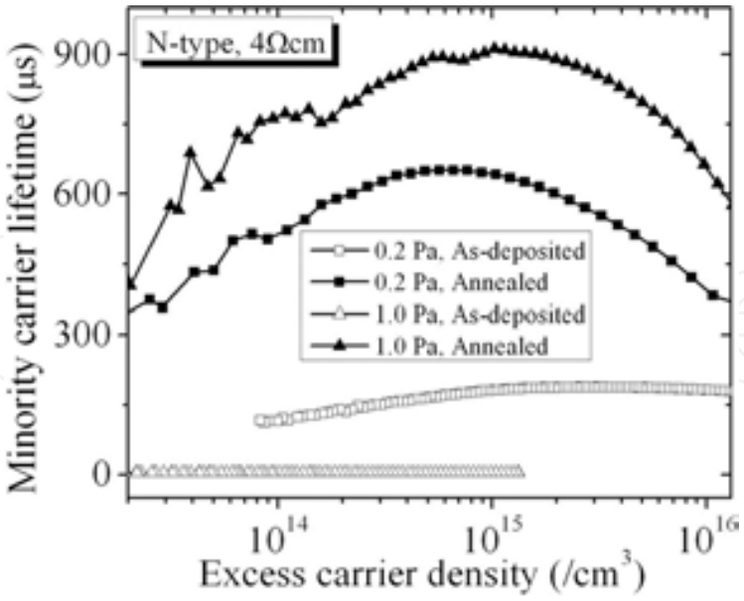

Figure 39. Injection level-dependent lifetime curves of the n-type 4 Ωcm c-Si passivated by a-Si:H deposited under different working pressures.

Figure 40 shows the lifetime curves in two types of c-Si substrates passivated by a-Si:H deposited under two temperature points of RT and 140 °C. For the p-type 2 Ωcm c-Si substrate, substrate temperature does not strongly influence the lifetime curve. In comparison, increasing temperature from RT to 140 °C deteriorates the lifetime value severely in n-type 4 Ωcm c-Si substrate. This difference is possibly from the different conductivity values which strongly influence temperature-dependent hydrogen diffusion on the surface or at the interface. The detailed mechanism needs further study to clarify.

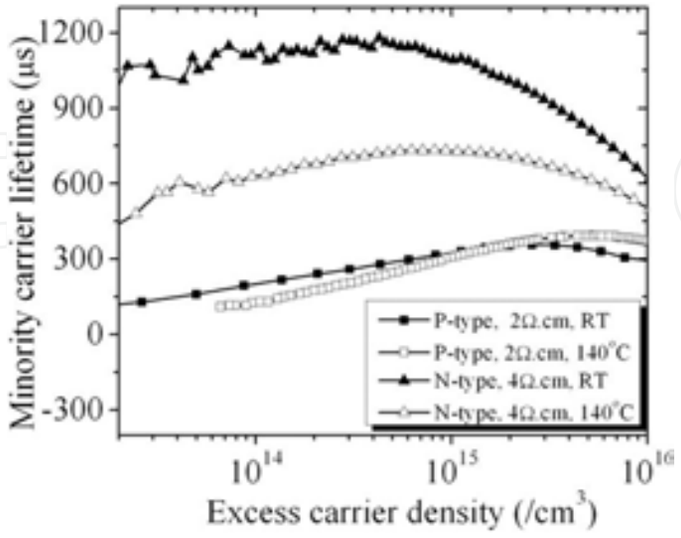

Figure 40. Injection level-dependent lifetime curve of two types of c-Si substrates passivated by a-Si:H deposited under different substrate temperatures.

Figure 41 shows the best lifetime results we obtained in three types of c-Si substrates. At the excess carrier density of $10^{15}/cm^3$, the best lifetime values are 1.3 ms, 620 μs, and 290 μs for the n-type 4 Ωcm, p-type 2 Ωcm, and p-type 1 Ωcm c-Si substrates, respectively.

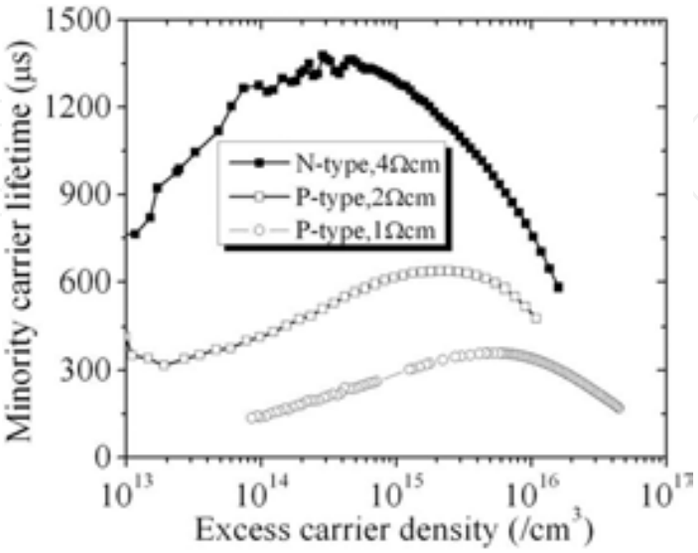

Figure 41. The best lifetime curves obtained in three types of c-Si substrates passivated by a-Si:H deposited in remote LFICP with an antenna-substrate distance of 53 cm.

3.4. c-Si passivation by stack configuration and implied V_{oc}

It is well known that the passivation effect is strongly dependent on the passivation layer thickness. In a practical HIT solar cell, the total thickness of deposited functional layer on one side is several tens of nanometers, less than the commonly used thickness of 50 nm in passivation studies. In addition, in a practical HIT solar cell, the passivation configuration is a stack of intrinsic and doped a-Si:H layers instead of above only intrinsic layer. Therefore, it is important to study the stack layer passivation configuration for the HIT solar cell applications. The passivation effect associated open-circuit voltage, namely, the implied V_{oc}, can be also determined from the QSSPC method. Using this method, we can estimate V_{oc} of the solar cell precursor (without the metallization procedure).

Intrinsic and doped a-Si:H films were symmetrically deposited on the p-type 1 Ωcm c-Si substrates to form the passivation configurations of n/i/P-c-Si/i/n or p/i/P-c-Si/i/p. This stack passivation scheme combines the chemical passivation (by intrinsic a-Si:H) and the field passivation (by doped a-Si:H). As an example, **Figure 42** shows the field passivation by p-a-Si:H in (a) and the combination of both passivation mechanisms in (b). Addition of a p-doped layer introduces an additional electrical filed to hinder the minority diffusion to the surface. The barrier Φ_{BSF} exponentially reduces the concentration of minority at the interface and thus the surface recombination. In **Figure 42(b)**, the interface defect density is reduced by the chemical passivation of addition of an intrinsic layer. Then, the solar cell precursor with the structure of n/i/P/i/p was fabricated to estimate the lifetime values. In these structures, the

http://dx.doi.org/10.5772/63529

intrinsic and doped layer thicknesses are about 5 and 15 nm, respectively, estimated from the average deposition rate at corresponding deposition conditions. **Figure 43** shows the lifetime curves in different passivation configurations. Lifetime value τ_{eff} in p/i/P/i/p is much lower than that in n/i/P/i/n. It is reported that B dopant is prone to react with Si atom to form complex, increasing the interface defect density [80].

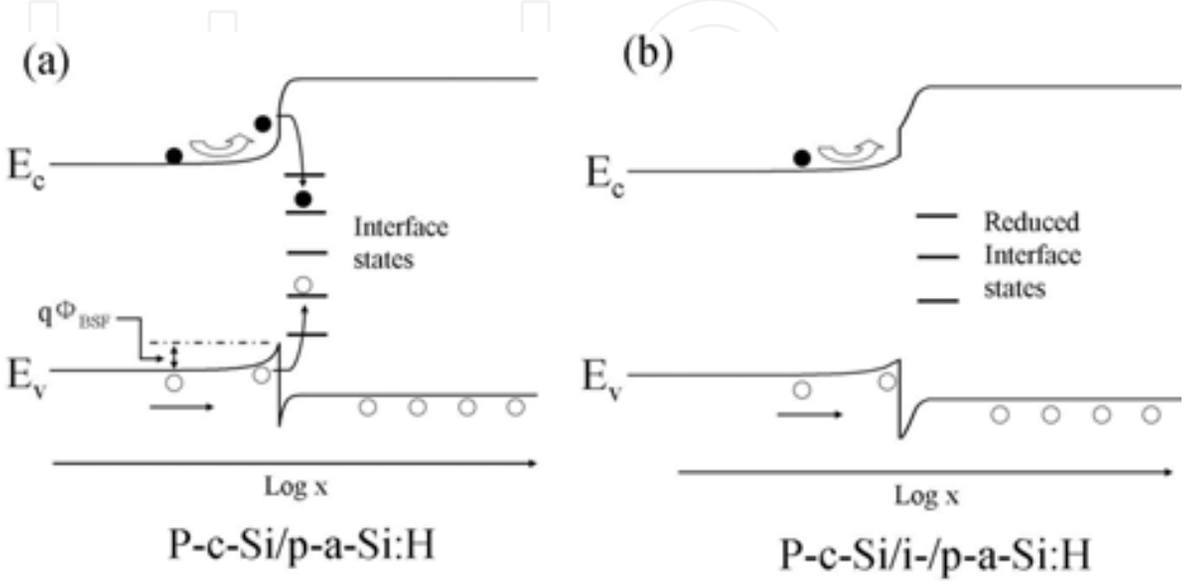

Figure 42. The filed passivation created by p-doped a-Si:H (a), and the combination of chemical surface passivation and field passivation in a stack of an intrinsic and p-doped layer (b).

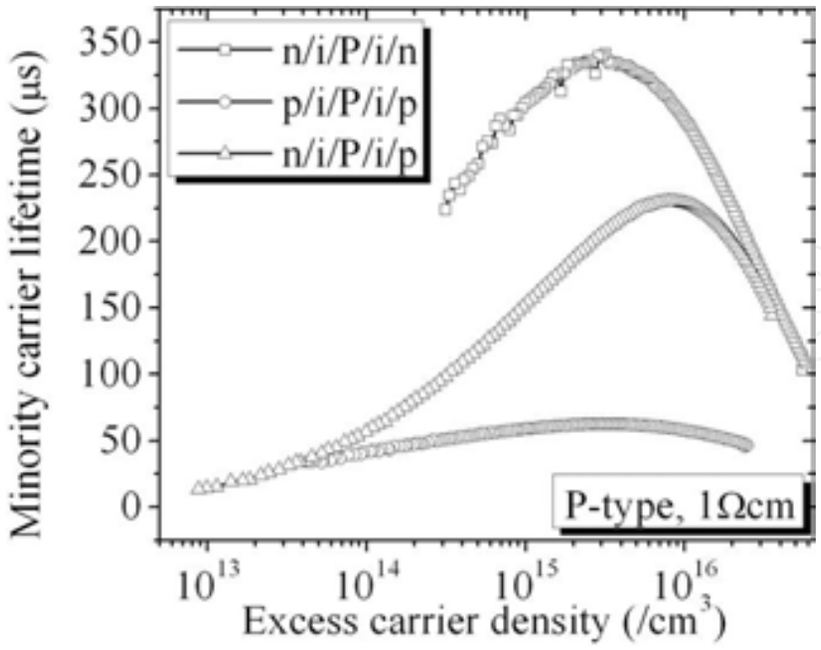

Figure 43. The injection level-dependent lifetime values in the p-type 1 Ωcm c-Si passivated by symmetric and asymmetric structures consisting of intrinsic and doped a-Si:H.

The relation between V_{oc} and effective lifetime τ_{eff} can be expressed as [81]:

$$V_{oc} = \frac{kT}{q} \ln \frac{2J_{ph}\tau_{eff}(N_A + \Delta n)}{qn_i^2 W} \tag{7}$$

where J_{ph} is the photocurrent density, N_A the background dopant density, and n_i the intrinsic carrier concentration in silicon. As expected, a high lifetime value corresponds to a high V_{oc}. In our p-type 1 Ωcm Si (thickness of 300 μm), the implied V_{oc} is about 670 and 620 mV corresponding to the solar cell precursor (n/i/P/i/p) lifetime of 150 and 64 μs, respectively.

4. Conclusions

As a low-temperature plasma source, LFICP has the inherent advantages of high-density plasma, low sheath potential, and low electron temperature, etc., which deserves an excellent CVD route. In LFICP CVD, the parameters of the RF power, hydrogen dilution, working pressure, and substrate temperature significantly influence the microstructures and properties of the films. The ion bombardment on the growing surface in LFICP CVD can be effectively controlled by the parameter of antenna-substrate distance *d*, providing an additional way to tune the microstructures and properties of Si-based materials.

The passivation effects of LFICP CVD Si-based materials are strongly dependent on the plasma configuration. In a region not far away the plasma generation area (semi-remote LFICP), the passivated c-Si shows a high as-deposited carrier lifetime due to the hydrogen-related chemical annealing during the deposition process. However, the additional thermal annealing does not lead to a considerable increase in the lifetime value. The addition of CO_2 into the reactive gases substantially influences the microstructure of the obtained thin films and improves the interface quality. In the region far away from plasma generation region (with a high antenna-substrate distance, remote-LFICP), a-Si:H passivated c-Si shows a low as-deposited and a high post-deposition annealing lifetime value. The highest lifetime value of 1.3 ms after thermal annealing is obtained in passivated 4 Ωcm c-Si substrate. After being passivated by the device-like scheme of undoped/doped silicon film stack, p-type substrate (1 Ωcm, 300 μm) shows an implied open voltage of 670 mV.

Acknowledgements

This work was jointly supported by AcRF Tier1 (No. RP 6/13 XS), A*STAR, Singapore, and the National Science Foundation of China (Grant No. 51302028 and 61404061).

Author details

H. P. Zhou[1,2*], S. Xu[2*] and S. Q. Xiao[3]

*Address all correspondence to: haipzhou@uestc.edu.cn; shuyan.xu@nie.edu.sg

1 School of Energy Science and Engineering, University of Electronic Science and Technology of China, Chengdu, Sichuan, China

2 Plasma Sources and Application Center, NIE, and Institute of Advanced Studies, Nanyang Technological University, Singapore

3 Key Laboratory of Advanced Process Control for Light Industry (Ministry of Education), Department of Electronic Engineering, Jiangnan University, Wuxi, Jiangsu, China

References

[1] Panasonic HIT Solar Cell Achieves World's Highest Energy Conversion Efficiency of 25.6% at Research Level Internet] 2014. Available from: http://news.panasonic.com/press/news/official.data/data.dir/2014/04/en140410-4/en140410-4.html

[2] Olibet S, Monachon C, Hessler A, Vallat-Sauvalin. E, Wolg De, Fesquet L, Damon-Lacoste J, Ballif C. Textured silicon heterojunction solar cells with over 700 mV open-circuit voltage studied by transmission electron microscopy. In: 23th European Photovoltaic Solar Energy Conference, Valencia, Spain; 2008. p. 1140

[3] Roschek T, Repmann T, Muller J, Rech B, Wagner H. Comprehensive study of micro-crystalline silicon solar cells deposited at high rate using 13.56 MHz plasma-enhanced chemical vapor deposition. Journal of Vacuum Science and Technology A. 2002; 20:492-498. DOI: 10.1116/1.1450585

[4] Ostrikov K. Reactive plasmas as a versatile nanofabrication tool. Review of Modern Physics. 2005; 77:489-511. DOI: http://dx.doi.org/10.1103/RevModPhys.77.489

[5] Amanatides E, Mataras D. Frequency variation under constant power conditions in hydrogen radio frequency discharges. Journal of Applied Physics, 2001; 89:1556-1566. DOI: 10.1063/1.1337597

[6] Rakhimova TV, Braginsky OV, Ivanov VV, Kim TK, Kong JT, Kovalev AS, Lopaev DV, Mankelevich YuA, Proshina OV, Vasilieva AN. Experimental and theoretical study of RF plasma at low and high frequency. IEEE Transactions on Plasma Science. 2006; 34:867- 877. DOI: 10.1109/TPS.2006.875849

[7] Rech B, Repmann T, van den Donker MN, Berginski M, Kilper T, Hüpkes J, Calnan S, Stiebig H, Wieder S. Challenges in microcrystalline silicon based solar cell technology. Thin Solid Films, 2006; 511:548-555. DOI: 10.1016/j.tsf.2005.12.161

[8] Xu S, Levchenko I., Huang SY, Ostrikov K. Self-organized vertically aligned single-crystal silicon nanostructures with controlled shape and aspect ratio by reactive plasma etching. Applied Physics Letters, 2009; 95:111505. DOI: 10.1063/1.3232210

[9] Denysenko I. B., Xu S., Long J. D., Rutkevych P. P., Azarenkov N. A. and Ostrikov K. Inductively coupled $Ar/CH_4/H_2$ plasma for low-temperature deposition of ordered carbon nanostructures. J. Appl. Phys. 2004; 95: 2713-2724. DOI: 10.1063/1.1642762

[10] Xiao SQ, Xu S, Ostrikov K. Low-temperature plasma processing for Si photovoltaics. Materials Science and Engineering R. 2014; 78:1-29. DOI: 10.1016/j.mser.2014.01.002

[11] Xu S, Ostrikov K, Li Y, Tsakadze EL, Jones IR. Low-frequency, high-density, inductively coupled plasma sources: operation and applications. Phys. Plasmas. 2001; 8: 2549-2557. DOI: 10.1063/1.1343887

[12] Ostrikov K, Xu S, Xu MY. Power transfer and mode transitions in low-frequency inductively coupled plasmas. Journal of Applied Physics. 2000; 88:2268-2271. DOI: 10.1063/1.1289055

[13] Cheng QJ, Xu S, Long JD, Ni ZH, Rider AE, Ostrikov K. High-rate, low-temperature synthesis of composition controlled hydrogenated amorphous silicon carbide films in low-frequency inductively coupled plasmas. Journal of Physics D: Applied Physics. 2008; 41:055406. DOI:10.1088/0022-3727/41/5/055406

[14] Cheng QJ, Xu S, Long JD, Huang SY, Guo J. Homogeneous nanocrystalline cubic silicon carbide films prepared by inductively coupled plasma chemical vapor deposition. Nanotechnology. 2007; 18:465601. DOI: 10.1088/0957-4484/18/46/465601

[15] Cheng QJ, Xu S, Ostrikov K. Rapid, low-temperature synthesis of nc-Si in high-density, non-equilibrium plasmas: enabling nanocrystallinity at low hydrogen dilution. Journal of Material Chemistry. 2009; 19:5134-5140. DOI: 10.1039/b904227

[16] Zhou HP, Xu LX, Xu S, Huang SY, Wei DY, Xiao SQ, Yan WS, Xu M. On the conductivity type conversion of the p-type silicon exposed to low frequency inductively coupled plasma of $Ar+H_2$. Journal of Physics D: Applied Physics. 2010; 43:505402. DOI: 10.1088/0022-3727/43/50/505402.

[17] Xu S, Huang SY, Levchenko I, Zhou HP, Wei DY, Xiao SQ, Xu LX, Yan WS, Ostrikov K. Highly efficient silicon nanoarray solar cells by a single-step plasma-based process. Advanced Energy Materials, 2011; 1:373-376. DOI: 10.1002/aenm.201100085

[18] Xiao SQ, Xu S, Zhou HP, Wei DY, Huang SY, Xu LX, Sern CC, Guo YN, Khan S. Amorphous/crystalline silicon heterojunction solar cells via remote inductively coupled plasma processing. Applied Physics Letters. 2012; 100:233902. DOI: http://dx.doi.org/10.1063/1.4721642

[19] Zhou HP, Wei DY, Xu S, Xiao SQ, Xu LX, Huang SY, Guo YN, Khan S, Xu M. Crystalline silicon surface passivation by intrinsic silicon thin films deposited by low-frequency inductively coupled plasma. Journal of Applied Physics 2012; 112:013708. DOI: http://dx.doi.org/10.1063/1.4733701.

[20] Cheng QJ, Xu S, Ostrikov K. Controlled-bandgap silicon nitride nanomaterials: deterministic nitrogenation in high-density plasmas. Journal of Material Chemistry. 2010; 20:5853-5859. DOI: 10.1039/c0jm01060j

[21] Zhou HP, Wei DY, Xu LX, Guo YN, Xiao SQ, Huang SY, Xu S. Low temperature SiN_x:H films deposited by inductively coupled plasma for solar cell applications. Applied Surface Science. 2013; 264:21-26. DOI: 10.1016/j.apsusc.2012.09.050

[22] Zhou HP, Wei DY, Xu S, Xiao SQ, Xu LX, Huang SY, Guo YN, Khan S, Xu M. Si surface passivation by SiO_x:H films deposited by a low-frequency ICP for solar cell applications. Journal of Physics D: Applied Physics. 2012; 45:395401-395408. DOI: 10.1088/0022-3727/45/39/395401

[23] Droz C, Sauvain EV, Bailat J, Feitknecht L. Relationship between Raman crystallinity and open-circuit voltage in microcrystalline silicon solar cells. J. Meier and A. Shah, Sol. Energy Materials and Solar Cells. 2004; 81:61-71. DOI: 10.1016/j.solmat.2003.07.004

[24] Vetterl O, Finger F, Carius R, Hapke P, Houben L, Kluth O, Lambertz A, Mück A, Rech B, Wagner H. Intrinsic microcrystalline silicon: A new material for photovoltaics. Solar Energy Materials and Solar Cells. 2000; 62:97-108. DOI: 10.1016/S0927-0248(99)00140-3

[25] Li J, Wang J, Yin M, Gao P, He D, Chen Q, Li Y, Shirai H. Deposition of controllable preferred orientation silicon films on glass by inductively coupled plasma chemical vapor deposition. Journal of Applied Physics. 2008; 103:043505-1- 043505-7. DOI: 10.1063/1.2885158

[26] Shen C, Shieh J, Huang J. Y, Kuo H, Hsu C. W, Dai B, Lee C, Pan C, Yang F. Inductively coupled plasma grown semiconductor films for low cost solar cells with improved light-soaking stability. Applied Physics Letters. 2011; 99:033510-1- 033510-3 DOI: 10.1063/1.3615650

[27] Huang J, Lin C, Shen C, Shieh J, Dai B. Low cost high-efficiency amorphous silicon solar cells with improved light-soaking stability. Solar Energy Materials and Solar Cells. 2012; 98:277-282. DOI: 10.1016/j.solmat.2011.11.023

[28] Sakikawa N, Shishida Y, Miyazaki S, Hirose M. High-rate deposition of hydrogenated amorphous silicon films using inductively coupled silane plasma. Solar Energy Materials and Solar Cells. 2001; 66:337-343. DOI: 10.1016/S0927-0248(00)00192-6

[29] Kosku N, Kurisu F, Takegoshi M, Takahashi H, Miyazake S. High-rate deposition of highly crystallized silicon films from inductively coupled plasma. Thin Solid Films. 2003; 435:39-43. DOI: 10.1016/S0040-6090(03)00374-2

[30] Dao VA, Duy NV, Heo J, Choi H, Kim Y, Lakshminarayan, Li J. Hydrogenated amorphous silicon layer formation by inductively coupled plasma chemical vapor

deposition and its application for surface passivation of p-type crystalline silicon. Japan Journal of Applied Physics. 2009; 48:066509-1-066509-4. DOI: 10.1143/JJAP.48.066509

[31] Mott NF, Davis EA. Electronic Processes in Non-Crystalline Solids. second ed., Clarendon, Oxford; 1979. 590 p.

[32] Matsuda A, Yamaoka T, Wolff S, KoyamaM, Imanishi Y, Kataoka H, Matsuura H, Tanaka K. Preparation of highly photosensitive hydrogenated amorphous Si-C alloys from a glow-discharge plasma. Journal of Applied Physics. 1986; 60:4205-4207. DOI: 10.1063/1.337528

[33] Zhou HP, Wei DY, Xu S, Xiao SQ, Xu LX, Huang SY, Guo YN, Yan WS, Xu M. Dilution effect of Ar/H_2 on the microstructures and photovoltaic properties of nc-Si:H deposited in low frequency inductively coupled plasma. Journal of Applied Physics. 2011; 110:023517. DOI: 10.1063/1.3605288

[34] Saha JK, Bahardoust B, Leong K, Gougam AB, Kherani N, Zukotynski S. Spectroscopic ellipsometry studies on hydrogenated amorphous silicon thin films deposited using DC saddle field plasma enhanced chemical vapor deposition system. Thin Solid Films. 2011; 519:2863-2866. DOI: 10.1016/j.tsf.2010.12.074

[35] Cavalcoli D, Rossi M, Cavallini A. Defect states in nc-Si:H films investigated by surface photovoltage spectroscopy. Journal of Applied Physics. 2011; 109:053719-1-053719-5. DOI: 10.1063/1.3553583

[36] Bagolini L, Mattoni A, Colombo L. Electronic localization and optical absorption in embedded silicon nanograins. Applied Physics Letters. 2009; 94:053115-1-053115-3. DOI: 10.1063/1.3078281

[37] Smit C, van Swaaij RACM, Donker H, Petit AMHN, Kessels WMM, van de Sanden MCM. Determining the material structure of microcrystalline silicon from Raman spectra. Journal of Applied Physics. 2003; 94:3582-3588. DOI: 10.1063/1.1596364

[38] Myong SY, Lim KS, Konagai M. Effect of hydrogen dilution on carrier transport in hydrogenated boron-doped nanocrystalline silicon-silicon carbide alloys. Applied Physics Letters. 2006; 88:103120. DOI: 10.1063/1.2177641

[39] Cheng QJ, Xu S, Ostrikov K. Temperature-dependent properties of nc-si thin films synthesized in low-pressure, thermally nonequilibrium, high-density inductively coupled plasmas. Journal of Physics and Chemistry C. 2009; 113:14759-14764. DOI: 10.1021/jp9047083

[40] Solomon I, Drévillon B, Shirai H, Layadi N. Plasma deposition of microcrystalline silicon: the selective etching model. 15th International Conference on Amorphous Semiconductors: Science and Technology; 6-10 September 1993; Cambridge: Journal of Non-Crystalline Solids. 1993; 164–166: 989-992.

[41] Kaxiras E, Joannopoulos JD. Hydrogenation of semiconductor surfaces: Si and Ge (111). Physical Review B.1988; 37:8842-8848. DOI: http://dx.doi.org/10.1103/PhysRevB.37.8842

[42] Smets AHM, Matsui T, Kondo M. Infrared analysis of the bulk silicon-hydrogen bonds as an optimization tool for high-rate deposition of microcrystalline silicon solar cells. Applied Physics Letters. 2008; 92:033506. DOI: 10.1063/1.2837536

[43] Spear WE, Le Comber PG. Substitutional doping of amorphous silicon. Solid State Communications. 1975; 17:1193-1196. DOI:10.1016/0038-1098(75)90284-7

[44] Street RA. Hydrogenated Amorphous Silicon. Cambridge University Press; 1991. 417 p. DOI: 10.1017/CBO9780511525247

[45] Winer K, Street RA, Johnson NM, Walker J. Impurity incorporation and doping efficiency in a -Si:H. Physics Review B. 1990; 42:3120-3128. DOI: http://dx.doi.org/10.1103/PhysRevB.42.3120

[46] Michaelis W, Pilkuhn MH. Radiative recombination in silicon p-n junctions. Physics State Solids. 1969; 36:311-319. DOI: 10.1002/pssb.19690360132

[47] Ashcroft NW, Mermin ND. Solid State Physics. Brooks/Cole Thomson Learning. 1976. 826 p.

[48] Shockley W, Read WT. Statistics of the recombination of holes and electrons. Physics Review. 1952; 87:835-842. DOI: http://dx.doi.org/10.1103/PhysRev.87.835

[49] Hall RN. Electron-hole recombination in germanium. Physics Review. 1952; 87:387-387. DOI: http://dx.doi.org/10.1103/PhysRev.87.387

[50] Schroder DK. Semiconductor Material and Device Characterization. John Wiley & Sons, Inc; 1990. 755 p. DOI: 10.1002/0471749095

[51] Aberle AG. Surface passivation of crystalline silicon solar cells: a review. Progress in Photovoltaics. 2000; 8:473-487. DOI: 10.1002/1099-159X(200009/10)8:5<473:AID-PIP337>3.0.CO;2-D

[52] Descoeudres A, Barraud L, Bartlome R, Choong G, Wolf SD, Zicarelli F, Ballif C. The silane depletion fraction as an indicator for the amorphous/crystalline silicon interface passivation quality. Applied Physics Letters. 2010; 97:183505. DOI: http://dx.doi.org/10.1063/1.3511737

[53] Kerr MJ, Schmidt J, Cuevas A, Bultman JH. Surface recombination velocity of phosphorus-diffused silicon solar cell emitters passivated with plasma enhanced chemical vapour deposited silicon. Journal of Applied Physics. 2001; 89:3821-3826. DOI: http://dx.doi.org/10.1063/1.1350633

[54] Kerr MJ, Cuevas A. Very low bulk and surface recombination in oxidized silicon wafers. Semiconductor Science Technology. 2002; 17:35-38. DOI: http://dx.doi.org/10.1088/0268-1242/17/1/306

[55] Martín I, Vetter M, Orpella A, Voz C, Puigdollers J, Alcubilla R. Characterization of a-SiCx:H films for c-Si surface passivation. Applied Physics Letters. 2002; 81:476-479. DOI: http://dx.doi.org/10.1557/PROC-715-A24.5

[56] Fujiwara H, Kondo M. Effects of a-Si:H layer thicknesses on the performance of a-Si:H/c-Si heterojunction solar cells. Journal of Applied Physics. 2007; 101:054516. DOI: 10.1063/1.2559975

[57] Wang Q, Page MR, Iwaniczko E, Xu Y, Roybal L, Baure R, To B, Yuan HC, Duda A, Fasoon F, Yan YF., Levi D, Meier D, Branz HM, Wang TH. Efficient heterojunction solar cells on p-type crystal silicon wafers. Applied Physics Letters. 2010; 96:013507. DOI: 10.1063/1.3284650

[58] Lee JY, Glunz SW. Investigation of various surface passivation schemes for silicon solar cells. Solar Energy Matters & Solar Cells. 2006; 90:82-92. DOI: 10.1016/j.solmat.2005.02.007

[59] Schmidt J, Kerr M, Cuevas A. Surface passivation of Si solar cells using plasma-enhanced chemical vapor deposited SiN films and thermal SiO2/thermal SiN Stacks. Semiconductor Science Technology. 2001; 19:164-170. DOI: 10.1088/0268-1242/16/3/308

[60] Martin I, Vetter M, Orpella A, Puidollers J, Cuevas A, Alcublla R. Surface passivation of p-type crystalline Si by plasma enhanced chemical vapor deposited amorphous SiCx:H films. Applied Physics Letters. 2001; 79:2199-2201. DOI: 10.1063/1.1404406

[61] Dauwe S, Schmid J, Hezel R. Very low surface recombination velocities on p- and n-type silicon wafers passivated with hydrogenated amorphous silicon films. Proceedings of the Photovoltaic Specialists Conference; 19–24 May 2002; New York: IEEE; 2002. p. 1246-1249.

[62] Willem J, Schuttauf A, Van der Werf KHM, Kielen IM, Van Sark WGJHM, Rath JK, Schropp REI. High quality crystalline silicon surface passivation by combined intrinsic and n-type hydrogenated amorphous silicon. Applied Physics Letters. 2011; 98:153514. DOI: 10.1063/1.3662404

[63] Vetterl O, Finger F, Carius R, Hapke P, Houben L, Kluth O, Lambertz A, Mück A, Rech B, Wagner H. Intrinsic microcrystalline silicon: a new material for photovoltaics. Solar Energy Materials Solar Cells. 2000; 62:97-108. DOI: 10.1016/S0927-0248(99)00140-3

[64] Rem JB, Holleman J, Verweij JF. Incubation time measurements in thin-film deposition. Journal of Electrochemical Society. 1997; 144:2101-2106. DOI: 10.1149/1.1837748

[65] Tickle AC. Thin-Film Transistors: A New Approach to Microelectronic. John Wiley & Sons, New York; 1969. 144 p.

[66] Mitchell J, Macdonald D, Cuevas A. Thermal activation energy for the passivation of the n-type crystalline silicon surface by hydrogenated amorphous silicon. Applied Physics Letters. 2009; 94:162102. DOI: 10.1063/1.3120765

[67] Rath J K. Low temperature polycrystalline silicon: a review on deposition, physical properties and solar cell applications. Solar Energy Materials Solar Cells. 2003; 76:437-487. DOI: 10.1016/S0927-0248(02)00258-1

[68] Strahm B, Howling A, Sansonnens L, Hollenstein C. Fast equilibration of silane/hydrogen plasmas in large area RF capacitive reactors monitored by optical emission spectroscopy. Plasma Sources Science Technology. 2007; 16:679-696. DOI: 10.1088/0963-0252/16/4/001

[69] Fujiwara H, Kaneko T, Kondo M. Application of hydrogenated amorphous silicon oxide layers to c-Si heterojunction solar cells. Applications of Physics Letters. 2007; 91:133508. DOI: 10.1063/1.2790815

[70] Sritharathikhun J, Banerjee C, Otsubo M, Sugiura T, Yamamoto H, Sato T, Limmanee A, Yamada A, Konagai M. Surface passivation of crystalline and polycrystalline silicon using hydrogenated amorphous silicon oxide film. Japan Journal of Applied Physics. 2007; 46:3296-3300. DOI: 10.1143/JJAP.46.3296

[71] Mueller T, Schwertheim S, Fahrner WR. Crystalline silicon surface passivation by high-frequency plasma-enhanced chemical-vapor-deposited nanocomposite silicon suboxides for solar cell applications. Journal of Applied Physics. 2010; 107:014504 DOI: 10.1063/1.3264626

[72] Bulkin PV, Swart PL, Lacquet BM. Electron cyclotron resonance plasma enhanced chemical vapour deposition and optical properties of SiOx thin films. Journal of Non-Crystalline Solids. 1998; 226:58-66. DOI: 10.1016/S0022-3093(98)00362-7

[73] Colberg SK, Barkmann N, Streich C, Schütt A, Suwito D, Schäfer P, Müller S, Borchert D. 26th European PV Solar Energy Conference and Exhibition; 5-9 September 2011; Hamburg: EU PVSEC Proceedings; 2011. p. 1770-1773.

[74] Jana T, Mukhopadhyay S, Ray S. Low temperature silicon oxide and nitride for surface passivation of silicon solar cells. Solar Energy Materials and Solar Cells. 2002; 71:197-211. DOI: 10.1016/S0927-0248(01)00058-7

[75] Watanabe H, Haga K, Lohner T. Structure of high-photosensitivity silicon oxygen alloy-films. 15th International Conference on Amorphous Semiconductors: Science and Technology; 6-10 September 1993; Cambridge: Journal of Non-Crystalline Solids; 1993. p. 1085-1088.

[76] Sritharathikhun J, Yamamoto H, Miyajima S, Yamada A, Konagai M. Optimization of amorphous silicon oxide buffer layer for high-efficiency p-type hydrogenated microcrystalline silicon oxide/n-type crystalline silicon heterojunction solar cells. Japan Journal of Applied Physics. 2008; 47:8452-8455. DOI: 10.1143/JJAP.47.8452

[77] Banerjee C, Sritharathikhun J, Yamada A, Konagai M. Fabrication of heterojunction solar cells by using microcrystalline hydrogenated silicon oxide film as an emitter.

Journal of Applied Physics D: Applied Physics. 2008; 41:185107. DOI:10.1088/0022-3727/41/18/185107

[78] Chen MS, Santra AK, Goodman DW. Structure of thin SiO_2 films grown on Mo(112). Physics Review B. 2004; 69:1124-1133. DOI: http://dx.doi.org/10.1103/PhysRevB.69.155404

[79] Sze SM. Semiconductor Devices: Physics and Technology, John Wiley & Sons; 2002. 576 p.

[80] Wolf SD, Kondo M. Nature of doped a-Si:H/c-Si interface recombination. Journal of Applied Physics. 2009; 105:103707-103707-6. DOI: 10.1063/1.3129578

[81] Sinton RA, Cuevas A. Contactless determination of current–voltage characteristics and minority-carrier lifetimes in semiconductors from quasi-steady-state photoconductance data. Journal of Applied Physics. 1996; 69:2510-2512. DOI: S0003-6951(96)02743-X